



HAL
open science

The endoplasmic reticulum in perisynaptic astrocytic processes: shape, distribution and effect on calcium activity

Audrey Denizot, María Fernanda Veloz Castillo, Pavel Puchenkov, Corrado Calì, Erik de Schutter

► To cite this version:

Audrey Denizot, María Fernanda Veloz Castillo, Pavel Puchenkov, Corrado Calì, Erik de Schutter. The endoplasmic reticulum in perisynaptic astrocytic processes: shape, distribution and effect on calcium activity. 2022. hal-03591633v1

HAL Id: hal-03591633

<https://hal.science/hal-03591633v1>

Preprint submitted on 28 Feb 2022 (v1), last revised 8 Apr 2022 (v2)

HAL is a multi-disciplinary open access archive for the deposit and dissemination of scientific research documents, whether they are published or not. The documents may come from teaching and research institutions in France or abroad, or from public or private research centers.

L'archive ouverte pluridisciplinaire **HAL**, est destinée au dépôt et à la diffusion de documents scientifiques de niveau recherche, publiés ou non, émanant des établissements d'enseignement et de recherche français ou étrangers, des laboratoires publics ou privés.

The endoplasmic reticulum in perisynaptic astrocytic processes: shape, distribution and effect on calcium activity

Audrey Denizot ^{1*}, María Fernanda Veloz Castillo ², Pavel Puchenkov ³,
Corrado Cali ^{4,5}, Erik De Schutter ¹

¹ Okinawa Institute of Science and Technology, Computational Neuroscience Unit, Onna-Son, Japan

² Biological and Environmental Science and Engineering Division, King Abdullah University of Science and Technology, Thuwal, Saudi Arabia

³ Okinawa Institute of Science and Technology, Scientific Computing and Data Analysis section, Research Support Division, Onna-Son, Japan

⁴ Department of Neuroscience, University of Torino, Italy

⁵ Neuroscience Institute Cavalieri Ottolenghi, Orbassano, Italy

*To whom correspondence should be addressed; E-mail: audrey.denizot3@oist.jp.

1 **Neurotransmission triggers Ca^{2+} signals in perisynaptic astrocytic processes**
2 **(PAPs). As most PAPs are below the diffraction limit, the presence of Ca^{2+}**
3 **stores in PAPs, notably the endoplasmic reticulum (ER), is unclear. Here, we**
4 **create 46 three dimensional meshes of hippocampal tripartite synapses recon-**
5 **structed from electron microscopy. We find that 75 % of PAPs contain some**
6 **ER, as close as 72 nm to the synapse, and quantify its geometrical properties.**
7 **To discern the effect of ER shape and distribution on Ca^{2+} activity, we imple-**
8 **mented an algorithm that automatically redistributes the ER within the recon-**
9 **structed PAP meshes, with constant ER and PAP shape. Reaction-diffusion**
10 **simulations in those meshes reveal that Ca^{2+} signals in PAPs are shaped by**
11 **a complex interplay between the clustering of Ca^{2+} channels, Ca^{2+} buffering,**
12 **ER shape and distribution. This study, by detecting ER in PAPs and linking its**
13 **spatial properties to Ca^{2+} activity, sheds new light on mechanisms regulating**
14 **signal transmission at tripartite synapses.**

15 Introduction

16 Astrocytes are glial cells of the central nervous system that are essential to numerous brain func-
17 tions (1). Notably, astrocytes are key modulators of neurotransmission at so-called tripartite
18 synapses (2, 3). A single astrocyte in the CA1 region of the mouse hippocampus is in contact
19 with hundreds of thousands of synapses simultaneously, at perisynaptic astrocytic processes
20 (PAPs) (4). Around 75 % of cortical and 65 % of hippocampal synapses are contacted by an
21 astrocytic process (5, 6). This close contact between astrocytes and neurons allows astrocytes to
22 control various synaptic functions, from glutamate uptake (7) and spillover (8, 9), to synapse
23 homeostasis (10), stability (11), synaptogenesis (12) and neurotransmission (3, 13). Those
24 synaptic functions are associated with specific local molecular expression in PAPs (14, 15),
25 which changes upon fear conditioning (14). Importantly, the alteration of the proximity of
26 PAPs to hippocampal synapses of the CA1 region *in vivo* affects neuronal activity and cognitive
27 performance (9). Conversely, neuronal activity has been shown to induce the remodeling of
28 synaptic coverage by PAPs in various brain regions, *in vivo* and in acute slices (6, 8, 11, 16–20).
29 Together, those results illustrate that PAPs are preferential sites of neuron-astrocyte commu-
30 nication. The recent emergence of super-resolution techniques has provided key insights into
31 the properties and functions of PAPs (21, 22). Yet, our understanding of PAP physiology and
32 function in live tissue is hindered by the nanoscopic size of most PAPs (23, 24).

33
34 Ca^{2+} signals are commonly interpreted as a measure of astrocyte activity, notably in re-
35 sponse to neurotransmitter release at synapses (23, 25, 26). The recent advances in Ca^{2+} imag-
36 ing approaches has allowed to improve the spatio-temporal resolution of Ca^{2+} signals in astro-
37 cytes (26, 27). Strikingly, it revealed that astrocytes in acute slices and *in vivo* exhibit spatially-
38 restricted Ca^{2+} signals, also referred to as hotspots or microdomains, stable over time and
39 which activity varies under physiological conditions such as locomotion or sensory stimula-
40 tion (28–40). Growing evidence supports that PAPs are preferential sites displaying spatially-
41 restricted Ca^{2+} microdomains in response to neurotransmission (28, 38, 39, 41, 42). As a single
42 astrocyte can contact hundreds of thousands of synapses simultaneously (4), such spatially-
43 restricted Ca^{2+} microdomains might enable the astrocyte to finely tune synaptic transmission at
44 the single synapse level.

45
46 mGluR activation on the astrocytic membrane following neurotransmission at glutamater-
47 gic synapses results in Ca^{2+} transients mediated by G_q proteins and Ca^{2+} stores such as the
48 endoplasmic reticulum (ER) (27). Most astrocytic Ca^{2+} signals are mediated by the Inositol 3-
49 Phosphate (IP_3) receptors on the membrane of the endoplasmic reticulum (ER) (43). Because
50 of their nanoscopic size, the Ca^{2+} pathways involved in microdomain Ca^{2+} signals in PAPs are
51 still unclear. Notably, the presence of ER in PAPs and its involvement in microdomain Ca^{2+}
52 signals at synapses is highly debated. During the last decade, PAPs have indeed been regarded
53 as devoid of ER, with a minimum distance between the synapse and the closest astrocytic ER $>$
54 $0.5 \mu\text{m}$ (23, 44). In contrast, inhibiting ER-mediated Ca^{2+} signaling in fine processes results in a

55 decreased number of Ca^{2+} domains (30) and a decreased Ca^{2+} peak frequency (30, 37, 42). Fur-
56 thermore, some astrocytic ER has been detected near synapses in other EM studies (24, 45, 46).
57 Yet, the geometrical properties of the ER in PAPs and its distribution remain poorly character-
58 ized, but could have a strong impact on neuron-astrocyte communication at tripartite synapses.

59
60 Here, we use a $220 \mu\text{m}^3$ hippocampal astrocytic volume from the CA1 stratum radiatum
61 region (6 nm voxel resolution) (47), reconstructed from electron microscopy (EM), to create 46
62 three dimensional meshes of tripartite synapses. Strikingly, we find that 75 % of PAPs contain
63 some ER, which can be as close as 72 nm to the post-synaptic density (PSD). Analysis of the
64 geometrical features of those meshes reveal the vast diversity of ER shapes and distributions
65 within PAPs from a single cell. We then used a detailed stochastic reaction-diffusion model of
66 Ca^{2+} signals in PAPs to investigate the mechanistic link between the spatial features of the ER
67 measured in the 3D meshes and the spatio-temporal properties of Ca^{2+} microdomain activity
68 in PAPs. To be able to decipher the effect of ER distribution within the PAP independently
69 from the effect of its shape, we developed an algorithm that automatically creates realistic 3D
70 tetrahedral PAP meshes with various ER distributions from the realistic meshes reconstructed
71 from EM. *In silico* experiments in those meshes reveal that the spatio-temporal properties of
72 Ca^{2+} signals in PAPs are tightly regulated by a complex interplay between the clustering of
73 Ca^{2+} channels, the ratio between ER surface area and PAP volume, Ca^{2+} buffering and ER
74 spatial distribution. Together, this study provides new insights into the geometrical properties
75 of hippocampal tripartite synapses and predicts mechanistic links between those features and
76 Ca^{2+} microdomain activity at tripartite synapses.

77 **Results**

78 **Quantification of the main geometrical properties of hippocampal tripar-** 79 **tite synapses**

80 To characterize the presence, shape and distribution of the endoplasmic reticulum (ER) in
81 perisynaptic astrocytic processes (PAPs), we used a $220 \mu\text{m}^3$ ($7.07 \mu\text{m} \times 6.75 \mu\text{m} \times 4.75 \mu\text{m}$)
82 hippocampal astrocytic volume from the CA1 stratum radiatum region reconstructed from a
83 perfectly isotropic EM stack (6 nm voxel resolution) (47). Elements from the neuropil, i.e. bou-
84 tons, dendritic spines and post-synaptic densities (PSDs), were also reconstructed. Following
85 the workflow presented in Fig. 1A, 44 excitatory and 2 inhibitory tripartite synapse meshes
86 were created, containing all elements belonging to the astrocyte and to the neuropil within a
87 $3.375 \mu\text{m}^3$ volume, corresponding to a cube of $1.5 \mu\text{m}$ edge length centered at the center of
88 mass of the PSD. Five of those tripartite synapse meshes are displayed in Fig. 1B. Among
89 those meshes, 16 were located at the borders of the $220 \mu\text{m}^3$ astrocytic volume. They were
90 thus omitted from data analysis as synaptic elements in those meshes could not be fully recon-
91 structed. The volume, surface area and surface-volume ratio (SVR) of each synaptic element,

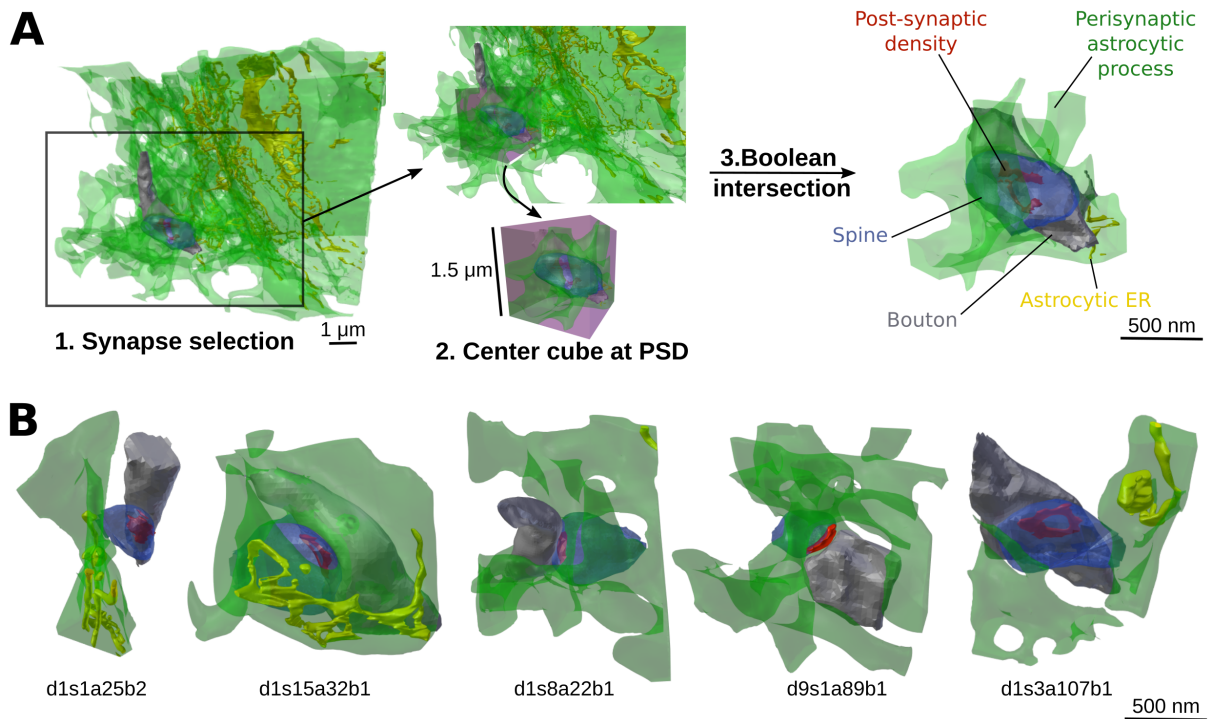


Fig 1: Reconstruction of 46 tripartite synapse meshes from electron microscopy. (A) Schematic presenting our tripartite synapse mesh creation workflow, here performed on synapse d10s1a2b1. 1. Synapses in contact with the $220 \mu\text{m}^3$ astrocytic volume were selected one by one. 2. A cube of $1.5 \mu\text{m}$ edge length ($3.375 \mu\text{m}^3$) was created and centered at the center of mass of the post-synaptic density (PSD, red). 3. Boolean intersection between the neuronal and astrocytic objects and the cube resulted in the isolation of the elements of the tripartite synapse mesh: the perisynaptic astrocytic process (PAP, green), the astrocytic endoplasmic reticulum (ER, yellow), the bouton (grey) and the spine (blue). This workflow resulted in the creation of 44 excitatory and 2 inhibitory tripartite synapse meshes. (B) Images of five of the 3D tripartite synapse meshes created, d1s1a25b2, d1s15a32b1, d1s8a22b1, d9s1a89b1, d1s3a107b1, revealing their diverse geometrical properties.

92 i.e the PAP, astrocytic ER, spine and bouton, of the remaining 28 fully reconstructed excitatory
93 tripartite synapses are presented in Fig. 2C-E and Supplemental Table S1. The minimum dis-
94 tance between each vertex on the membrane of the PAP and the center of mass of the PSD was
95 measured in each of the 28 meshes (Fig. 2B), providing a quantification of the distribution of
96 the astrocyte around the synapse. Our results highlight the diverse distances between PSDs and
97 PAPs belonging to a single cell. In accordance with previous studies (6, 44, 48), PAP membrane
98 vertices could be as close as 5 nm to the PSD, with an average distance between the PSD and
99 the closest PAP vertex of 65 nm. Importantly, we found that PM-PSD distance is the shortest,
100 i.e PAPs are the closest to the synapse, when bouton surface area is low (Fig. 2F, $p=0.013$).
101 PAP-PSD distance was not correlated to PAP (Fig. 2G, $p=0.14$) or spine (Fig. 2H, $p=0.24$)
102 surface area.

103 **Presence and geometrical properties of the endoplasmic reticulum in perisy-** 104 **naptic astrocytic processes**

105 Because of the small size of most PAPs, the Ca^{2+} pathways that regulate astrocytic Ca^{2+} mi-
106 crodomain activity at tripartite synapses remain to be uncovered. Notably, the presence of ER
107 in PAPs is controversial (24, 44–46). We have thus analyzed the presence and shape of the ER
108 in the PAPs from the 28 fully reconstructed excitatory tripartite synapse meshes presented in
109 Fig. 2.

110 75% of PAPs contained some ER (Fig. 3C), which challenges the widespread belief that tri-
111 partite synapses are devoid of astrocytic ER. ER surface area, volume and SVR were measured
112 in ER-containing PAPs and highlight that ER shape is highly variable between PAPs from the
113 same cell (Fig. 3B). Note that there was no significant difference between bouton, spine and
114 PAP surface area, volume and SVR between synapses with vs without astrocytic ER (Supple-
115 mental Fig. S1). We further characterized the vicinity of the astrocytic ER to the synapse. To do
116 so, we measured the distance between each vertex on the ER membrane to the center of mass
117 of the PSD ($n=21$). We found that ER-PSD distance varies drastically from synapse to synapse
118 (Fig. 3E) and can be as little as 72 nm, far below the $> 0.5 \mu\text{m}$ ER-PSD distance reported
119 previously (23, 44). The closest ER vertex was on average 432 nm away from the center of
120 mass of the PSD. Interestingly, the larger the surface area of the ER, the closer it was to the
121 PSD (Fig. 3F, $p=0.013$). Astrocytic ER was closer to the PSD in PAPs with higher surface
122 area (Fig. 3G, $p=0.024$). The minimum ER-PSD distance was not correlated to spine (Fig. 3H,
123 $p=0.54$) or bouton (Fig. 3I, $p=0.29$) surface area. Overall, our results highlight that most PAPs
124 contain some ER and that its shape is highly variable, which could have strong implications on
125 ER-dependent Ca^{2+} signaling in PAPs resulting from synaptic transmission.

126

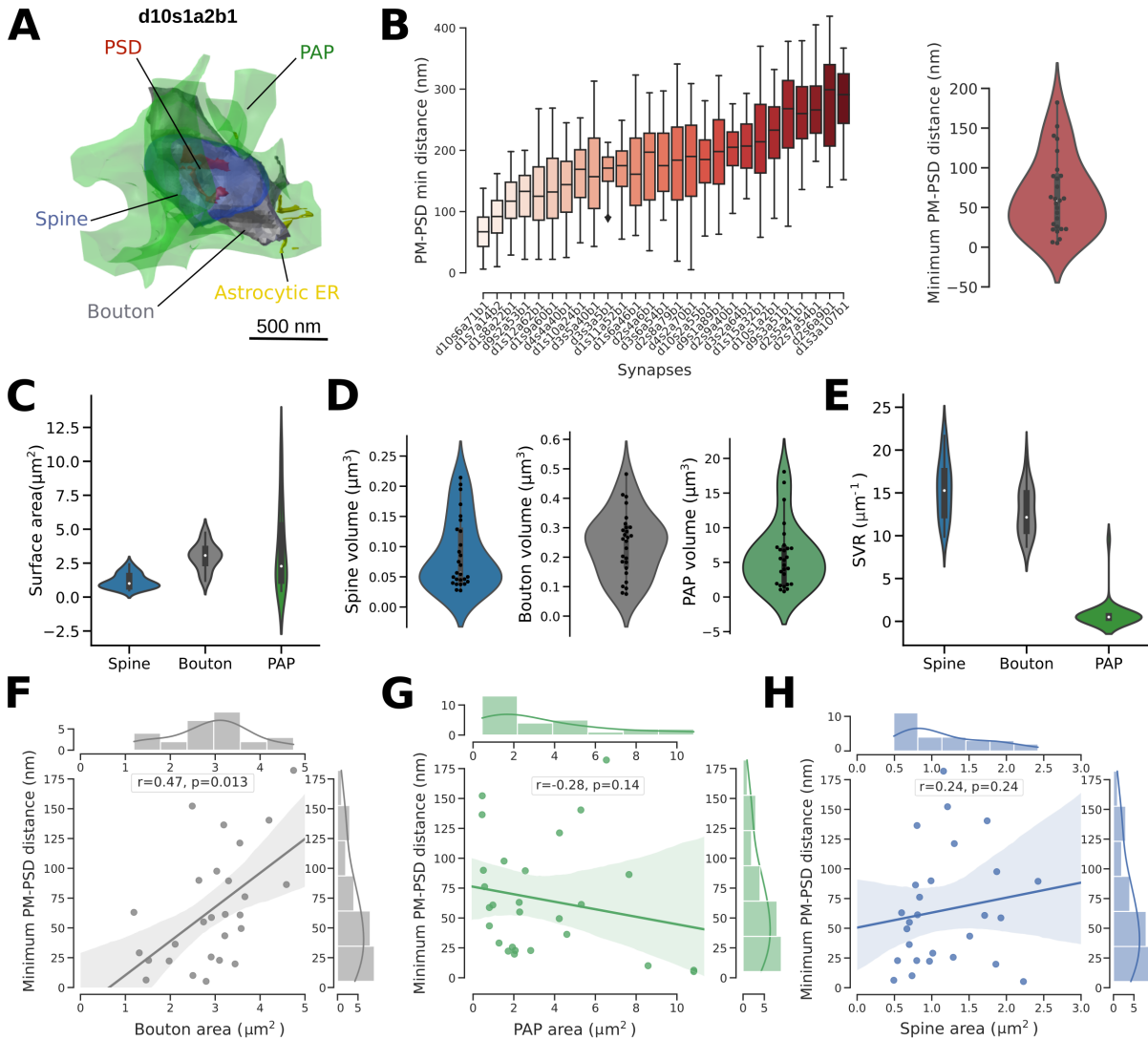


Fig 2: Characterization of the geometrical properties of hippocampal tripartite synapses.

(A) Image of a tripartite synapse mesh, d10s1a2b1, containing a bouton (grey), spine (blue), post-synaptic density (PSD, red), perisynaptic astrocytic process (PAP, green) and the astrocytic endoplasmic reticulum (ER, yellow). (B) Left: Boxplots presenting the distribution of the minimum distance between each vertex on the PAP membrane and the center of mass of the PSD, measured in the 28 excitatory tripartite synapse meshes fully reconstructed in this study. Right: Distribution of the minimum distance between the PAP and the PSD ($n=28$). (C-E) Violin plots presenting the distribution of spine, bouton and PAP surface area (C), volume (D) and surface-volume ratio (E). (F-H) Scatterplots presenting the variation of the minimum PAP-PSD distance as a function of bouton surface area (left), PAP surface area (middle) and spine surface area (right). Plots are presented with univariate kernel density estimation curves and a linear regression fit. Spearman correlation coefficients, r , and p -values, p , are displayed onto each regression plot, $n=28$.

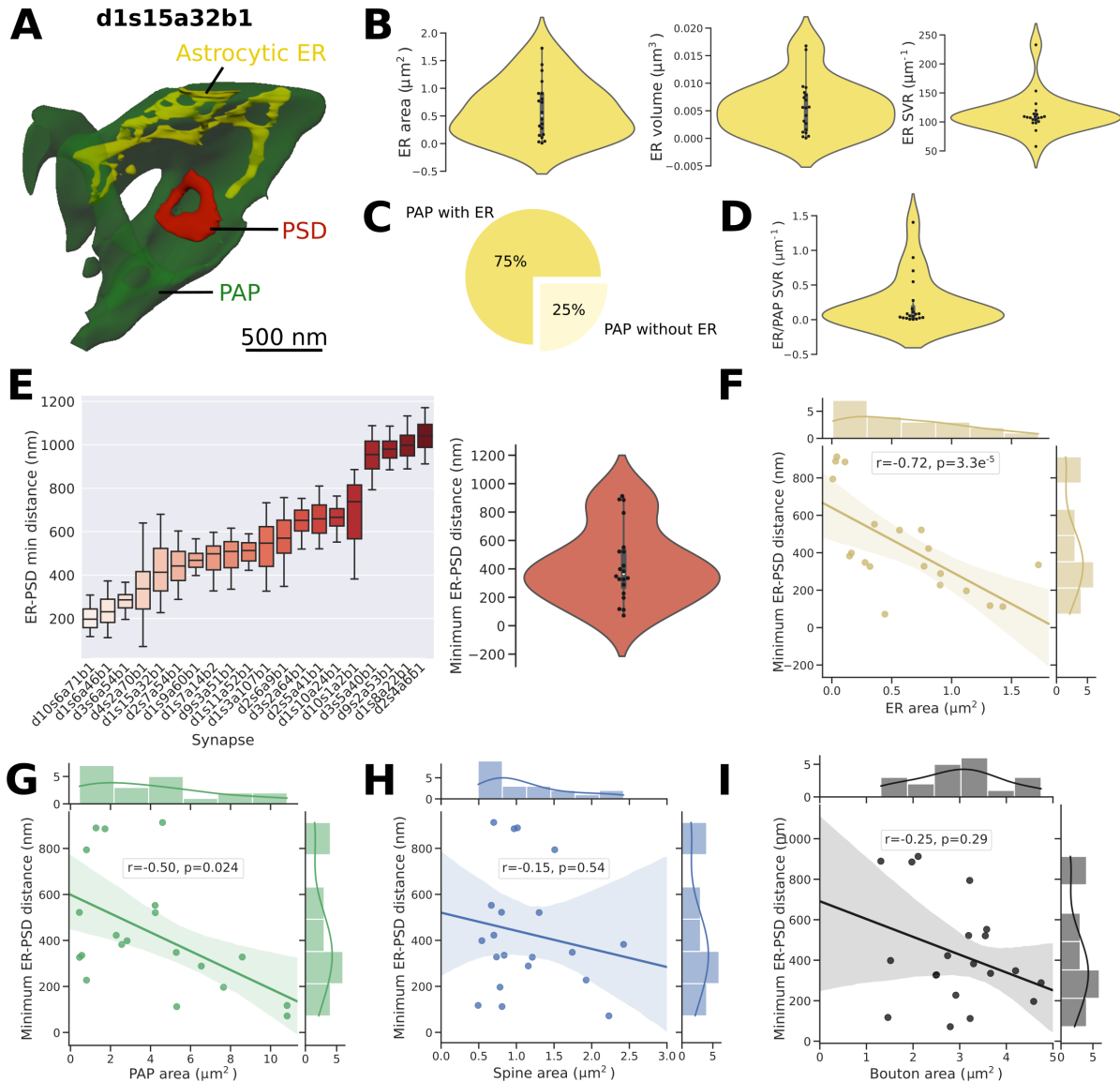


Fig 3: Presence and geometrical properties of the endoplasmic reticulum in perisynaptic astrocytic processes. (A) Image of the d1s15a32b1 PSD (red) and the neighboring PAP (green), that contains ER (yellow). (B) Violin plots representing the distribution of ER surface area (left), volume (middle) and surface volume ratio (right) within PAPs, $n=21$. (C) Among the 28 fully reconstructed PAP meshes extracted, 75 % contained some ER. (D) Distribution of the ratio between the ER surface area and PAP volume ($n=21$). (E) Quantitative analysis of the distance between the astrocytic ER and the neighboring PSD, $n=21$. (Left) Boxplots presenting the distribution of the distance of ER membrane vertices to the center of mass of the PSD in each PAP. (Right) Distribution of the minimum ER-PSD distance in PAPs, $n=21$. The lowest ER-PSD distance measured was 70nm (synapse d4s2a70b1).

Fig 3: (F-I) Scatterplots presenting the variation of the minimum ER-PSD distance as a function of ER surface area (F), PAP surface area (G), spine surface area (H) and bouton surface area (I), $n=21$. Plots are presented with univariate kernel density estimation curves and a linear regression fit. Spearman correlation coefficient, r , and p-value, p , are displayed onto each regression plot.

127 **Reaction-diffusion simulations reveal different spatio-temporal properties** 128 **of Ca^{2+} signals in PAPs of the same cell**

129 PAPs are characterized by highly diverse sizes and shapes of the ER (Fig. 3), which could
130 have strong implications on ER-mediated Ca^{2+} signals in PAPs. Because of their nanoscale,
131 measuring Ca^{2+} activity and deciphering the involvement of ER-mediated signals in individual
132 PAPs in live tissue is extremely challenging (26). A better understanding of the mechanistic
133 link between the geometrical properties of the ER and the spatio-temporal properties of Ca^{2+}
134 microdomain signals in PAPs is crucial, yet hard to test experimentally. Here, we use the PAP
135 meshes presented in Fig. 3 together with a spatial stochastic model of Ca^{2+} signaling adapted
136 from the model of Denizot and collaborators (49) to investigate the mechanistic link between
137 ER shape and Ca^{2+} microdomain activity in PAPs. Ca^{2+} influx in the PAP cytosol in the model
138 is mediated by Inositol 3-Phosphate (IP_3) receptors on the membrane of the ER and by Ca^{2+}
139 channels at the plasma membrane, Ch_{PM} . The reactions modeled are presented in Fig. 4A and
140 in the Methods section. Neuronal activity was simulated at $t=1\text{s}$ by infusing 50 IP_3 molecules
141 at the PM of the PAP. The implementation of this model with STEPS software (50) allows to
142 perform simulations in tetrahedral meshes in 3 spatial dimensions, such as the ones created in
143 this study. Representative Ca-GCaMP traces in a cylindrical mesh, corresponding to the con-
144 centration of Ca^{2+} bound to Ca^{2+} indicators added to the cytosol of the model, display similar
145 spatio-temporal characteristics to Ca^{2+} signals measured in organotypic hippocampal astrocytic
146 cultures (51) (Fig. 4A, right).

147
148 We performed simulations in six PAP meshes reconstructed from electron microscopy, char-
149 acterized by various geometrical properties of the ER: d1s3a107b1, d1s8a22b1, d1s10a24b1,
150 d2s6a9b1, d9s4a34b1 and d10s1a2b1 (Fig. 4B, Table 1). To do so, meshes were pre-processed
151 to allow their use in reaction-diffusion simulations. The pre-processing workflow is described in
152 Fig. 4C and in the Methods section, and produced 3D tetrahedral meshes from the 2D triangular
153 meshes reconstructed from EM. Screenshots of simulations performed in two realistic tetrahe-
154 dral PAP meshes are presented in Fig. 4B. Ca-GCaMP and free Ca^{2+} signals, in simulations
155 with and without Ca^{2+} indicators in the cytosol, respectively, were measured in d1s3a107b1,
156 d1s8a22b1, d1s10a24b1, d2s6a9b1, d9s4a34b1 and d10s1a2b1 PAP meshes. Representative
157 traces are displayed in Fig. 4E. Signals varied greatly depending on the mesh (Fig. 4F). Note
158 that, in accordance with previous studies (49, 52), Ca-GCaMP and free Ca^{2+} signals displayed
159 different spatio-temporal properties (Fig. 4F). Those results suggest that the diverse geometrical

Table 1: **Characteristics of the 3D PAP meshes used in the reaction-diffusion simulations.**

V_{cyt} is the cytosolic volume, S_{PM} is the plasma membrane surface area, S_{ER} is the ER surface area, $\text{SVR}_{\text{ER/PAP}}$ is the ratio between the ER surface area and the cytosolic volume. ER_c is the number of ER vertices at ER-PM contact sites, i.e. ≤ 20 nm from the closest PM vertex. $d1s15a32b1_{f0}$, $d1s15a32b1_{f21}$, $d1s15a32b1_{f64}$ and $d1s15a32b1_{f250}$ refer to meshes from frames 0, 21, 64 and 250 of the $d1s15a32b1$ PAP mesh presented in Fig. 8-9.

Geom	$V_{\text{cyt}} (\mu\text{m}^3)$	$S_{\text{PM}} (\mu\text{m}^2)$	$S_{\text{ER}} (\mu\text{m}^2)$	$\text{SVR}_{\text{ER/PAP}} (\mu\text{m}^{-1})$	ER_c
$d1s3a107b1$	0.112	2.00	0.315	2.81	183
$d1s8a22b1$	0.397	8.60	0.031	0.078	31
$d1s10a24b1$	0.331	5.80	0.344	1.04	0
$d2s6a9b1$	0.505	10.0	0.273	0.54	158
$d9s4a34b1$	0.410	7.05	0.807	1.97	20958
$d10s1a2b1$	0.531	10.0	0.136	0.26	3771
$d1s15a32b1_{f0}$	0.426	6.91	0.85	2.00	295
$d1s15a32b1_{f21}$	0.426	6.91	0.85	2.00	2337
$d1s15a32b1_{f64}$	0.426	6.91	0.85	2.00	1683
$d1s15a32b1_{f250}$	0.426	6.91	0.85	2.00	2408
PAP1_v	0.434	3.55	0.088	0.21	0
PAP1_w	0.432	3.55	0.428	0.99	0
PAP1_x	0.428	3.55	0.834	1.95	125
PAP1_y	0.423	3.55	1.27	3.00	0
PAP1_z	0.418	3.55	1.62	3.88	555

160 features of PAPs and ER reported in this study (Fig. 2-3) strongly influence Ca^{2+} microdomain
 161 activity at tripartite synapses.

162 **The effect of IP₃R clustering differs from PAP to PAP**

163 IP₃R channels are not randomly distributed on the surface of the ER and form stable clusters of
 164 various sizes (53–56). Numerous computational studies performed in 2 spatial dimensions have
 165 predicted that IP₃R cluster size shapes Ca^{2+} activity (see (57) for a review). Whether this effect
 166 still holds in 3D, notably in complex shapes such as that of the PAPs reconstructed in this study,
 167 remains to be uncovered. We thus next simulated Ca^{2+} signaling in the 6 realistic PAP meshes
 168 presented in Fig. 4, reconstructed from EM, $d1s3a197b1$, $d1s8a22b1$, $d1s10a24b1$, $d2s6a9b1$,
 169 $d9s4a34b1$ and $d10s1a2b1$, with various distributions of IP₃Rs on the membrane of the ER.

170 Simulations of the model were performed with different IP₃R cluster sizes η . Ca^{2+} chan-
 171 nels were either randomly placed on the membrane of the PAP ($\text{cocl}=0$) or clustered onto the
 172 PM triangles that were the closest to the ER triangles containing an IP₃R cluster ($\text{cocl}=1$), em-
 173 ulating co-localization of Ca^{2+} channels, reported in neurons and astrocytes (58). As IP₃R

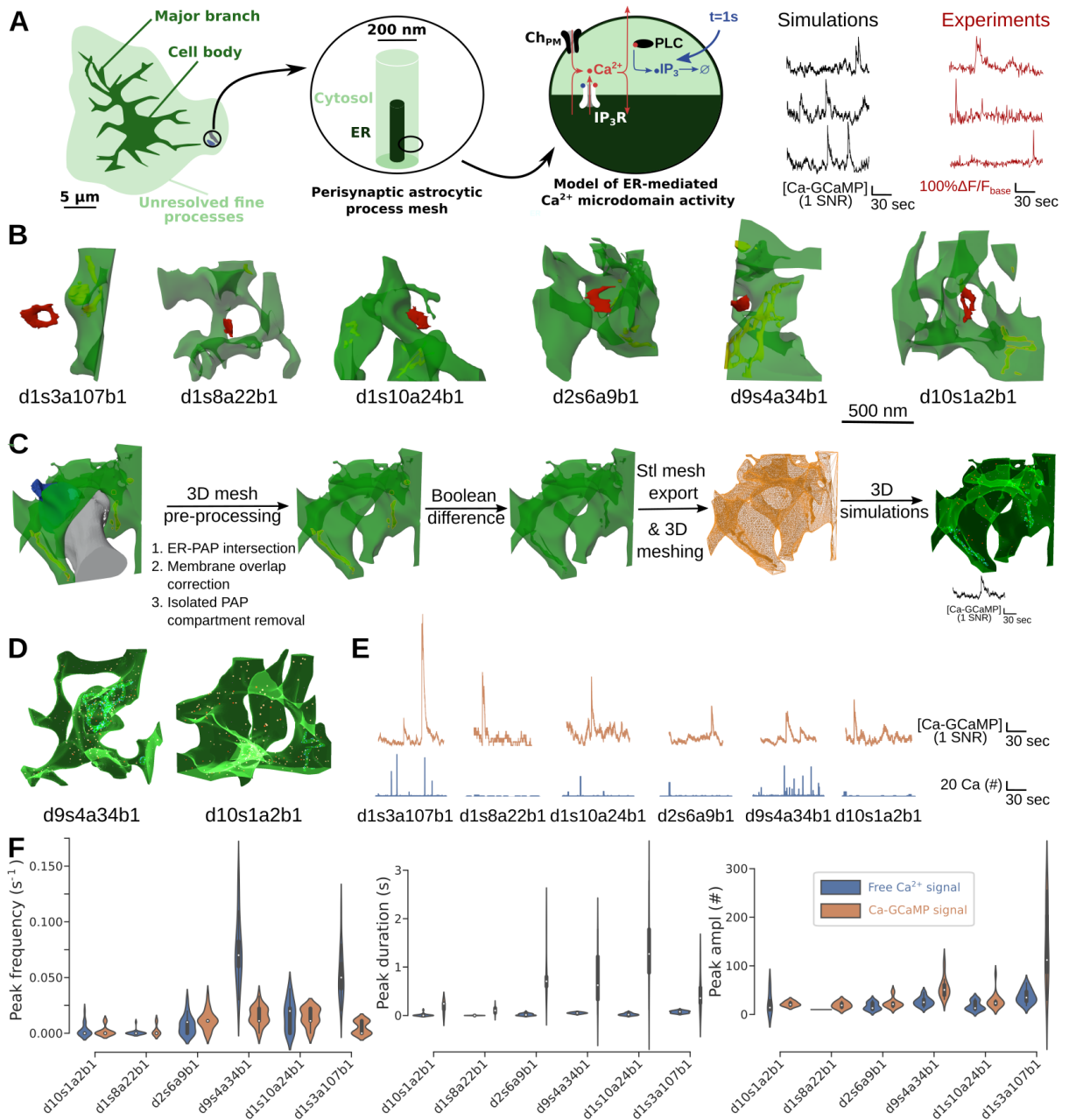


Fig 4: Reaction-diffusion simulations reveal different spatio-temporal properties of Ca²⁺ signals between PAPs of the same cell. (Left) Schematic representation of the model of Ca²⁺ signaling in PAPs used in this study. The model is stochastic, spatially-extended and simulations can be performed in 3D meshes. Ca²⁺ influx into the cytosol results from Ca²⁺ channels on the plasma membrane and from IP₃R channels on the ER. At t=1s, 50 IP₃ molecules were injected at the plasma membrane of the PAP, simulating neuronal activity. (Right) Representative Ca-GCaMP traces from simulations in a cylindrical mesh, 200 nm in diameter, 1 μm long (left, black) and experiments (right, red) (51).

Fig 4: (B) Images representing the 6 PAP meshes in which simulations were performed: d1s3a197b1, d1s8a22b1, d1s10a24b1, d2s6a9b1, d9s4a34b1 and d10s1a2b1. (C) Workflow to prepare the PAP meshes for 3D simulations illustrated on d2s6a9b1 mesh (see Methods section). The geometrical features of the resulting PAP meshes are presented in Table 1. (D) Screenshots of simulations in PAP meshes d9s4a34b1 and d10s1a2b1. Note that the darker and lighter greens result from 3D shading and rendering of the meshes. (E) Representative Ca-GCaMP (top, orange) and free Ca^{2+} (bottom, blue). Ca^{2+} traces were measured in separate simulations, where no GCaMP was added into the cytosol of the PAP. IP_3R channels and Ca^{2+} channels at the plasma membrane, Ch_{PM} , were randomly distributed onto the ER membrane and plasma membrane, respectively. (F) Quantification of peak frequency (left), duration (middle) and amplitude (right) of free Ca^{2+} (left, blue, n=20) and Ca-GCaMP (right, orange, n=20) signals measured *in silico* in 3D meshes of the PAPs presented in panel B.

174 density was kept constant across simulations, $3.5e^{-3}/\mu\text{m}^2$ (49), the total number of IP_3Rs ,
 175 $N_{\text{IP}_3\text{R}}$, varied depending on the mesh: 90, 230, 78, 8, 40 and 96 in PAP meshes from synapses
 176 d1s3a107b1, d9s4a34b1, d2s6a9b1, d1s8a22b1, d10s1a2b1 and d1s10a24b1, respectively. As
 177 IP_3R cluster size was a divider of $N_{\text{IP}_3\text{R}}$, cluster sizes tested varied slightly depending on the
 178 mesh. The range of IP_3R cluster size tested varied from $\eta=1-26$. Representative free Ca^{2+}
 179 traces measured in d1s3a197b1, d1s8a22b1, d1s10a24b1, d2s6a9b1, d9s4a34b1 and d10s1a2b1
 180 PAP meshes with various IP_3R cluster sizes η are displayed in Fig. 5B. Strikingly, IP_3R cluster-
 181 ing only affected Ca^{2+} activity in a subset of the PAP meshes studied (Fig. 5C). Indeed, Ca^{2+}
 182 peak duration and amplitude increased with IP_3R cluster size in PAP meshes from synapses
 183 d1s3a107b1 (ANOVA, $p=5.1e^{-5}$ and $1.9e^{-7}$), d2s6a9b1 (ANOVA, $p=3.16e^{-3}$ and 0.026) and
 184 d9s4a34b1 (ANOVA, $p=0.018$ and 0.028). This effect was associated with an increased fre-
 185 quency of IP_3R opening with cluster size (ANOVA, $p=3.4e^{-4}$, 0.007 and 0.037 in d1s3a107b1,
 186 d2s6a9b1 and d9s4a34b1, respectively). Those results highlight that different PAP and ER
 187 shapes are associated with different IP_3R clustering effects.

188

189 Interestingly, increased neuronal stimulation, simulated as an increased amount of IP_3 in-
 190 fused, i , in the PAP at $t=1\text{s}$, triggered clustering effects in a PAP in which no clustering effect
 191 was observed after a milder neuronal stimulation (Fig. 5D). This effect was characterized by an
 192 increase of Ca^{2+} peak amplitude (ANOVA, $p=8.2e^{-5}$ for $i=150$ and $p=4.66e^{-7}$ for $i=200$), fre-
 193 quency (ANOVA, $p=0.005$ for $i=150$ and $p=0.006$ for $i=200$) and duration (ANOVA, $p=3.4e^{-5}$
 194 for $i=150$, and $p=0.026$ for $i=200$) with IP_3R cluster size for $i=150$ and 200, while cluster size
 195 did not affect peak amplitude (ANOVA, $p=0.27$ for $i=50$ and $p=0.08$ for $i=100$), frequency
 196 (ANOVA, $p=0.86$ for $i=50$ and $p=0.72$ for $i=100$) and duration ($p=0.13$ for $i=50$ and $p=0.15$
 197 for $i=100$) for $i=50$ and 100. This effect was mediated by an increased IP_3R opening frequency
 198 with cluster size when neuronal stimulation was larger (ANOVA, $p=0.024$, $5.23e^{-7}$ and $7.8e^{-5}$,
 199 for $i=100$, 150 and 200, respectively), while clustering had no effect on IP_3R opening frequency
 200 for milder neuronal stimulation (ANOVA, $p=0.21$, $i=50$). This suggests that IP_3R clustering in

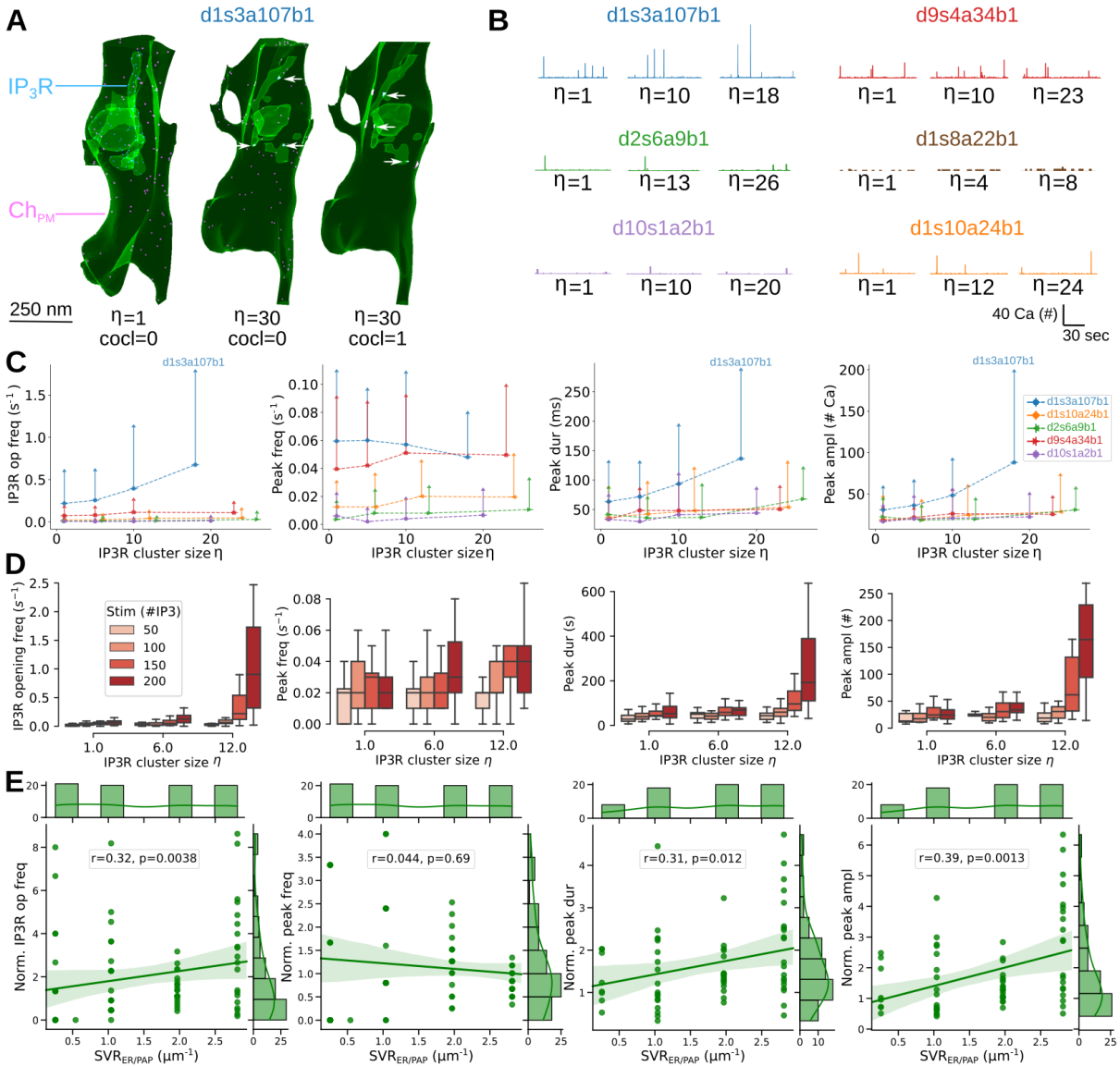


Fig 5: The effect of IP3R clustering differs from PAP to PAP. (A) Screenshots of simulations in d1s3a107b1, with IP₃R cluster size $\eta=1$ and $\eta=30$. Simulations were performed with (cocl=1) and without (cocl=0) co-clustering of Ca²⁺ channels at the plasma membrane (purple) with IP₃Rs on the ER (blue). IP₃R clusters are indicated with a white arrow. (B) Representative free Ca²⁺ traces measured *in silico* in d1s3a107b1 (blue), d9s4a34b1 (red), d2s6a9b1 (green), d1s8a22b1 (brown), d10s1a2b1 (purple) and d1s10a24b1 (orange) meshes. (C) Quantification of IP₃R opening frequency (left), Ca²⁺ peak frequency (middle left), duration (middle right) and amplitude (right) as a function of η , in d1s3a107b1 (blue circle), d1s10a24b1 (orange diamond), d2s6a9b1 (green triangle), d9s4a34b1 (red triangle) and d10s1a2b1 (purple hexagon), cocl=1. Data are represented as mean \pm STD, n=20 for each mesh and cluster size tested. (D) Quantification of IP₃R opening frequency (left), Ca²⁺ peak frequency (middle left), duration (middle right) and amplitude (right) as a function of IP₃R cluster size η , for different stimulation levels (Stim (#IP₃): 50, 100, 150, 200). (E) Normalized IP₃R opening frequency (left), peak frequency (middle left), duration (middle right) and amplitude (right) as a function of SVR_{ER/PAP} (μm^{-1}). Correlation coefficients (r) and p-values are shown for each plot.

Fig 5: Lines are guides for the eyes. Note that no peaks were detected in simulations in d1s8a22b1. (D) Quantification of IP₃R opening frequency (left), Ca²⁺ peak frequency (middle left), duration (middle right) and amplitude (right), in d1s10a24b1, for $\eta=1, 6$ and 12 and various levels of neuronal stimulation: IP₃ infused $i=50, 100, 150$ and 200 (from left to right, light red to dark red), $n=20$ for each parameter set tested. (E) Scatterplots presenting the variation of IP₃R opening frequency (left), Ca²⁺ peak frequency (middle left), duration (middle right) and amplitude (right) for $\eta=18-24$, normalized with Ca²⁺ peak characteristics measured for $\eta=1$, as a function of $SVR_{ER/PAP}$. Plots are accompanied by univariate kernel density estimation curves and a linear regression fit. Spearman correlation coefficient, r , and p-value, p , are displayed onto each regression plot.

201 PAPs could act as an amplifier of neuronal stimulation.

202

203 Unexpectedly, the PAPs in which an IP₃R clustering effect was observed were not the PAPs
 204 with the highest ER surface area S_{ER} , i.e with the highest number of IP₃R channels. Indeed,
 205 although the normalized IP₃R opening frequency and Ca²⁺ peak frequency at high cluster size
 206 were positively correlated with S_{ER} , normalized Ca²⁺ peak amplitude and duration were not
 207 correlated with S_{ER} (Supplemental Fig. S2). Rather, normalized IP₃R opening frequency,
 208 Ca²⁺ peak amplitude and duration were positively correlated to the ratio between ER surface
 209 area and PAP volume $SVR_{ER/PAP}$ (Fig. 5E, $p=0.0038, 0.012$ and 0.0013 , respectively). Ca²⁺
 210 peak frequency however did not vary with $SVR_{ER/PAP}$ (Fig. 5E, $p=0.69$). This probably re-
 211 sults from our peak definition. Indeed, as a peak is considered terminated when the Ca²⁺ trace
 212 decreases below peak threshold, a higher frequency of IP₃R opening events can result in suc-
 213 cessive opening events occurring before peak termination, resulting in a similar peak frequency
 214 but larger peak duration.

215

216 Overall, our simulation results nuance the effect of the clustering of Ca²⁺ channels on Ca²⁺
 217 signals in small sub-cellular compartments like PAPs. Strikingly, in contrast with reports from
 218 models in 2 spatial dimensions (57, 59), Ca²⁺ activity increased with cluster size in only a
 219 subset of the realistic 3D PAP meshes tested, highlighting the complex interplay between the ER
 220 surface to PAP volume ratio, the intensity of neuronal stimulation and IP₃R clustering on Ca²⁺
 221 microdomain activity. This highlights the importance of cautious interpretation of simulation
 222 results on geometrical effects depending on the geometry used.

223 **ER SVR conditions the amplification of Ca²⁺ activity by IP₃R clustering in** 224 **3D**

225 Our simulation results revealed that the increase of Ca²⁺ activity resulting from IP₃R cluster-
 226 ing increased with the ratio between the ER surface area and the PAP volume ($SVR_{ER/PAP}$, Fig
 227 5E). In the PAP meshes studied in Fig. 5, $SVR_{ER/PAP}$ varied together with PAP shape and ER

228 shape. To discern the effect of ER and PAP shape from $SVR_{ER/PAP}$ on Ca^{2+} activity in PAPs,
229 we created meshes with various ER size and constant ER and PAP shapes. The original mesh
230 was extracted from the $220 \mu m^3$ astrocytic volume, located at the vicinity of the d9s3a51b1
231 PSD and referred to as PAP1. The location of PAP1 in the $220 \mu m^3$ reconstructed hippocam-
232 pal astrocytic volume is presented in Supplemental Fig. S3. Meshes with various $SVR_{ER/PAP}$
233 were created from PAP1 by rescaling the ER using Blender software. Meshes were then created
234 following the mesh pre-processing workflow described in Fig. 4C, resulting in the creation of
235 $PAP1_v$, $PAP1_w$, $PAP1_x$, $PAP1_y$ and $PAP1_z$ meshes (Fig. 6A). The geometrical properties of
236 those meshes are presented in Table 1.

237
238 IP_3R opening frequency, Ca^{2+} peak frequency, duration and amplitude increased with
239 $SVR_{ER/PAP}$ (Fig. 6B-F). This is not surprising as ER surface area increases with $SVR_{ER/PAP}$
240 in those meshes, thus resulting in an increase of the amount of IP_3R channels with $SVR_{ER/PAP}$.
241 The total number of IP_3R channels, N_{IP_3R} , thus was 24, 120, 240, 360 and 460, in $PAP1_v$,
242 $PAP1_w$, $PAP1_x$, $PAP1_y$ and $PAP1_z$ meshes, respectively. Importantly, Ca^{2+} peak frequency
243 (Fig. 6D, ANOVA, $p=2.39e^{-8}$), duration (Fig. 6E, ANOVA, $p=7.52e^{-17}$) and amplitude (Fig.
244 6F, ANOVA, $p=1.29e^{-14}$) increased with IP_3R cluster size in $PAP1_z$ mesh. This resulted
245 from an increase of IP_3R opening frequency with cluster size in $PAP1_z$ (Fig. 6C, ANOVA,
246 $p=5.93e^{-24}$). No clustering effect was observed in $PAP1_{w-y}$ meshes, characterized by a lower
247 $SVR_{ER/PAP}$, confirming the mechanistic link between $SVR_{ER/PAP}$ and the amplification of
248 Ca^{2+} activity mediated by IP_3R clustering suggested in Fig. 5. Note that no Ca^{2+} signals were
249 detected in $PAP1_v$ mesh. Simulations in $PAP1_z$ meshes with constant IP_3R channel number
250 further highlight that this effect is mediated by $SVR_{ER/PAP}$ rather than by IP_3R channel density
251 (Supplemental Fig. S4). Supplemental Fig. S5 reveals that IP_3R opening frequency and Ca^{2+}
252 peak frequency increased with $SVR_{ER/PAP}$ even when IP_3R channels were not clustered ($\eta=1$).
253 Increasing ER surface area in PAP1 however also resulted in a decreased distance between the
254 ER and the plasma membrane (PM) in the PAP (Fig. 6G). Importantly, Ca^{2+} peak frequency
255 (Fig. 6H, $p=2.56e^{-11}$), duration (Fig. 6I, $p=2.18e^{-6}$) and amplitude (Fig. 6J, $p=1.32e^{-6}$) in-
256 creased with the amount of ER vertices at ER-PM contact sites (≤ 20 nm to the closest PM
257 vertex (60, 61)). This suggests that the increased IP_3R clustering effect on Ca^{2+} microdomain
258 activity in $PAP1_z$ could result either from its increased $SVR_{ER/PAP}$ or to the decreased ER-PM
259 distances in this mesh compared to $PAP1_{w-y}$ meshes. Overall, our simulation results suggest
260 that ER shape, notably the ratio between its surface area and PAP volume, shape astrocytic
261 Ca^{2+} microdomain activity at synapses.

262 **Quantification of ER-PM distance distribution within PAPs**

263 As simulation results suggested that Ca^{2+} activity in $PAP1_{v-z}$ meshes varies depending on
264 the distribution of the ER within the PAP, we next aimed at quantifying ER distribution in the
265 21 ER-containing PAP meshes reconstructed from EM and presented in Fig. 3. To do so,
266 we measured the distance between each vertex on the plasma membrane (PM) and the closest

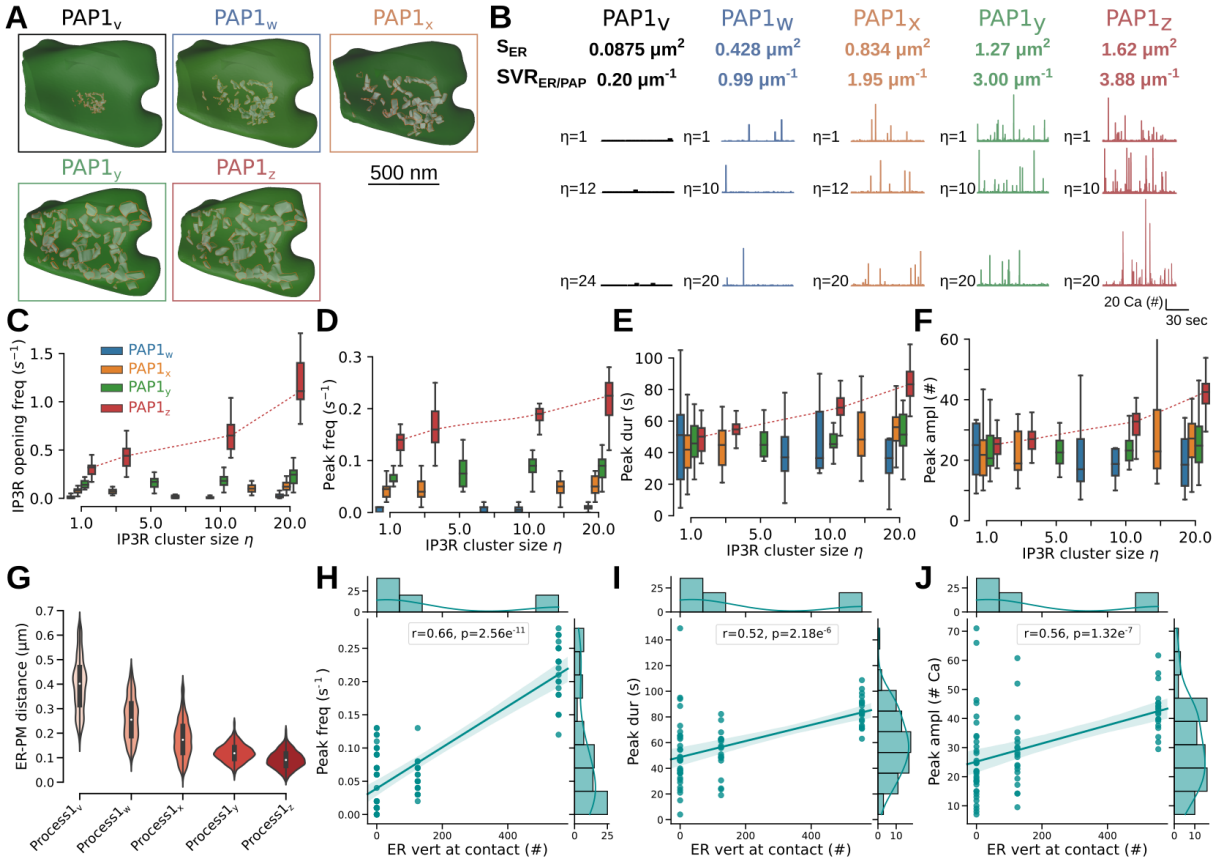


Fig 6: The surface-volume ratio of the ER in PAPs conditions the amplification of Ca^{2+} activity by IP_3R clustering in 3D. (A) Images of the different PAP meshes created to investigate the effect of the ratio between ER surface area and PAP volume, $SVR_{ER/PAP}$, on Ca^{2+} microdomain activity: PAP_{1v-z}. Meshes were obtained by rescaling the ER object in PAP1, located at the vicinity of the d9s3a51b1 PSD (Supplemental Fig. S3). Geometrical features of the meshes are presented in Table 1. (B) Representative free Ca^{2+} traces measured in PAP_{1v} (black), PAP_{1w} (blue), PAP_{1x} (orange), PAP_{1y} (green) and PAP_{1z} (red), for IP_3R cluster size $\eta=1$ (top), $\eta=12$ (middle) and $\eta=24$ (bottom). (C-F) Quantification of IP_3R opening frequency (C), Ca^{2+} peak frequency (D), duration (E) and amplitude (F), in PAP_{1w} (blue), PAP_{1x} (orange), PAP_{1y} (green) and PAP_{1z} (red), for $\eta=1-23$. Note that η varies depending on the mesh (see Methods). Lines were added to visualize the effect of η on Ca^{2+} peak characteristics in PAP_{1z} mesh. (G) Quantification of the variation of the distance between each ER vertex and the closest plasma membrane (PM) vertex in PAP_{1v-z} meshes. (H-J) Scatterplots presenting Ca^{2+} peak frequency (H), duration (I) and amplitude (J) in PAP_{1v-z} meshes for $\eta=20$, normalized with Ca^{2+} peak characteristics for $\eta=1$, as a function of the number of ER vertices ≤ 20 nm to the closest PM vertex.

Fig 6: Plots are presented with univariate kernel density estimation curves and a linear regression fit. Spearman correlation coefficient, r , and p-value, p , are displayed onto each regression plot.

267 vertex on the ER. We found that ER-PM distance is highly variable in PAPs from a single cell,
268 with an average ER-PM distance within a single PAP from around 200 nm to 1200 nm (Fig.
269 7B-C). Not surprisingly, mean ER-PM distance decreases as ER (Fig. 7D, $p=5.01e^{-10}$) and
270 PAP (Fig. 7E, $p=0.055$) surface area increase. Interestingly, ER-PM distance was lower in
271 PAPs contacting boutons with higher surface area (Fig. 7F, $p=0.022$). Note that there was no
272 correlation between ER-PM distance and spine surface area (Fig. 7G, $p=0.73$). Importantly,
273 we found that PAPs closer to the synapse are characterized by lower mean ER-PM distance
274 (Fig. 7H, $p=2.2e^{-5}$), which, according to simulation results presented in Fig. 6, could result in
275 enhanced Ca^{2+} activity in those PAPs.

276 **Effect of ER-PM distance in PAPs on Ca^{2+} microdomain activity**

277 To discern the effect of $SVR_{ER/PAP}$ from the effect of ER-PM distance on Ca^{2+} microdomain
278 activity in PAPs reported in Fig. 6, we implemented an algorithm that creates realistic tetra-
279 hedral 3D meshes of PAPs characterized by various distributions of the ER within the same
280 PAP. The workflow is presented in Fig. 8. Briefly, the ER is split into small portions of sim-
281 ilar size, then resized to match the total ER surface area of the original mesh. Simulations in
282 meshes with the original ER and with split ER confirmed that this ER splitting algorithm does
283 not alter Ca^{2+} activity in the PAP (Supplemental Fig. S6). A simulation of n frames is then
284 generated in Blender, which alters the location of the ER objects within the PAP. Each frame
285 is thus characterized by a unique distribution of the ER objects within the PAP, while ER and
286 PAP shape, surface area, volume and SVR are constant across frames (Supplemental movie 2).
287 The mesh processing workflow presented in Fig. 4C is then automatically applied to each frame
288 of interest. This workflow allows the creation of numerous realistic 3D PAP meshes, that can
289 be used for reaction-diffusion simulations in 3D. Fig. 7B-D displays the quantification of ER
290 distribution in the PAP meshes created with this workflow on PAP d1s15a32b1. The workflow
291 successfully produced realistic tetrahedral PAP meshes characterized by various ER-PM dis-
292 tances (Fig. 7B). Note that the distribution of ER-PM distance at ER-PM contact sites (ER-PM
293 distance ≤ 20 nm) did not vary, while the number of ER vertices belonging to contact sites, and
294 thus the size of the contact sites, increased with frame number (Fig. 7C).

295
296 To test the effect of ER distribution in PAPs, simulations were performed in meshes from
297 frames 0, 21, 64 and 250 of PAP d1s15a32b1 (Fig. 9A) with different IP_3R cluster sizes, η .
298 Free Ca^{2+} signals did not vary depending on ER distribution within the PAP (Fig. 9C). Inter-
299 estingly, ER distribution did not affect the amplification of IP_3R opening frequency (ANOVA,
300 $p=0.059$), Ca^{2+} peak duration (ANOVA, $p=0.55$) and amplitude (ANOVA, $p=0.15$) with IP_3R

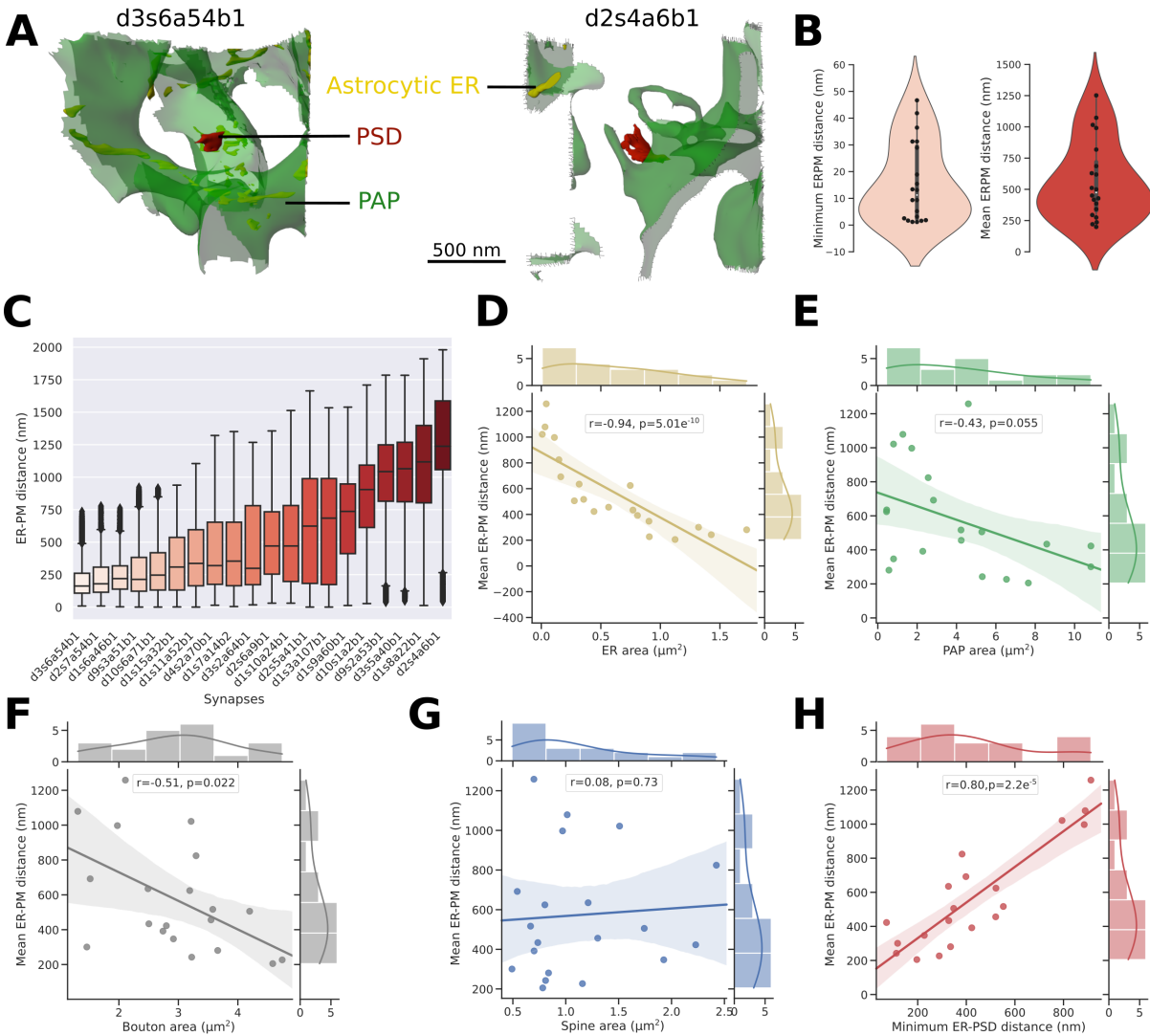


Fig 7: ER-PM distance in PAPs is highly variable and is decreased in PAPs close to the synapse. (A) Images of 2 PAP meshes (green), d3s6a54b1 (left) and d2s4a6b1 (right) with the neighboring PSD (red), displaying the diverse shapes and distributions of the ER (yellow) in PAPs from the same cell. (B) Distribution of the minimum (left) and mean (right) distance between each vertex on the plasma membrane (PM) and the closest ER vertex, measured in PAP meshes reconstructed from EM, $n=21$ (Fig. 3). (C) Quantification of the distance between each PM vertex and the closest ER vertex in each PAP mesh. (D-F) Scatterplots presenting the variation of the mean distance between each PM vertex and the closest ER vertex as a function of ER (D), PAP (E), bouton (F), spine (G) surface area and as a function of the minimum ER-PSD distance (H), $n=21$. Plots are presented with univariate kernel density estimation curves and a linear regression fit. Spearman correlation coefficient, r , and p -value, p , are displayed onto each regression plot.

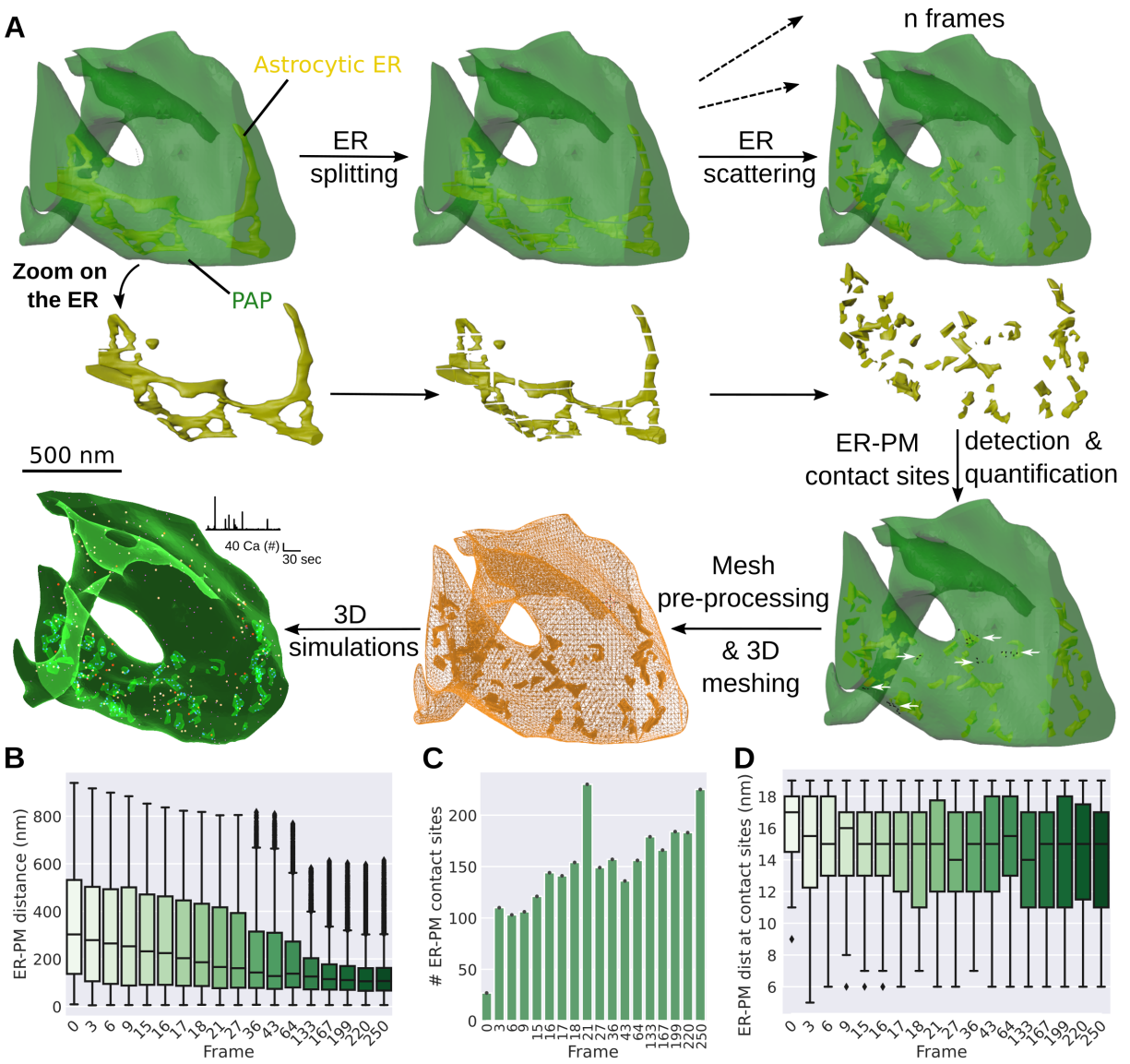


Fig 8: Automated realistic 3D PAP mesh generation with diverse ER distributions. (A) Schematic representing the workflow developed in this study to create realistic PAP meshes in 3 spatial dimensions with various ER distributions and constant shape, volume and surface area of PAP and ER, used on the PAP mesh d1s15a32b1. The ER is split and a simulation with n frames is generated in Blender, in which ER objects are subject to physical forces that alter their spatial distribution. The n frames are thus characterized by different locations of the ER elements within the PAP, with constant ER and PAP shapes. The pipeline detects, quantifies and exports in a text file the distance between each vertex at the plasma membrane (PM) and the closest vertex at the membrane of the ER. A point cloud can be created to visualize the ER vertices at ER-PM contact sites (ER-PM distance ≤ 20 nm, white arrows). The mesh pre-processing workflow presented in Fig. 4C is then applied to the mesh of each desired frame. The resulting 3D tetrahedral meshes can then be used for 3D reaction-diffusion simulations.

Fig 8: (B) Quantification of the distance between each PM vertex and the closest ER vertex in the meshes generated by the workflow presented in panel A, applied to the d1s15a32b1 PAP mesh. (C) Quantification of the number of ER vertices located at ER-PM contact sites, i.e ≤ 20 nm to the closest PM vertex, in each frame from mesh d1s15a32b1. (D) Quantification of the distance between each PM vertex and the closest ER vertex at ER-PM contact sites, in each frame from mesh d1s15a32b1.

301 cluster size when IP₃R clusters were randomly distributed on the membrane of the ER (Fig.
302 9D). However, the increase of peak frequency with cluster size was larger in meshes in which
303 the ER was closer to the plasma membrane (Fig 9D, ANOVA, $p=0.0048$). This suggests that
304 a distribution of the ER closer to the plasma membrane might allow increased Ca²⁺ peak fre-
305 quency with IP₃R cluster size.

306
307 As IP₃R clusters are believed to be preferentially located at ER-PM contact sites (54), we
308 performed simulations in the same meshes while positioning IP₃R clusters at ER-PM contact
309 sites. Screenshots of simulations with different locations of IP₃R clusters are presented in Fig.
310 9B. Interestingly, locating IP₃R clusters at ER-PM contact sites resulted in larger increases of
311 IP₃R opening frequency (ANOVA, $p=0.0019$) and Ca²⁺ peak frequency (ANOVA, $p=0.0043$)
312 with cluster size in meshes in which the ER was closer to the PM (Fig. 9D). However, the loca-
313 tion of the ER did not impact the effect of IP₃R cluster size on Ca²⁺ peak duration (ANOVA,
314 $p=0.45$) and amplitude (ANOVA, $p=0.069$). Together, those results suggest that a distribution
315 of the ER closer to the plasma membrane, coupled with a location of IP₃R clusters at ER-PM
316 contact sites, favors an increase of Ca²⁺ peak frequency with cluster size. ER-PM contact sites
317 could act as diffusional barriers. Locating IP₃R channels at ER-PM contact sites would thus
318 increase the residency time of Ca²⁺ ions and IP₃ molecules at the vicinity of the channels, thus
319 increasing the probability of Ca²⁺ and IP₃ binding to IP₃Rs and resulting in an increased IP₃R
320 opening frequency in meshes with larger ER-PM contact sites. To further test the interplay
321 between ER distribution, IP₃R clustering and local diffusional properties, Ca²⁺ buffers, here
322 Ca²⁺ indicators GCaMP6s, were added to the model. Strikingly, ER distribution had a greater
323 effect on buffered Ca²⁺ signals compared to free Ca²⁺ signals (Fig. 9E). More precisely, the in-
324 crease of IP₃R opening frequency (ANOVA, $p=2.37e^{-7}$), Ca-GCaMP peak frequency (ANOVA,
325 $p=1.14e^{-4}$), duration (ANOVA, $p=7.78e^{-3}$) and amplitude (ANOVA, $p=0.023$) with IP₃R clus-
326 ter size was significantly larger in meshes in which the ER was located closer to the plasma
327 membrane. Those results highlight that the effect of ER distribution within the PAP on Ca²⁺
328 microdomain activity is conditioned by the location of IP₃R channels at ER-PM contact sites
329 and by local Ca²⁺ buffering.

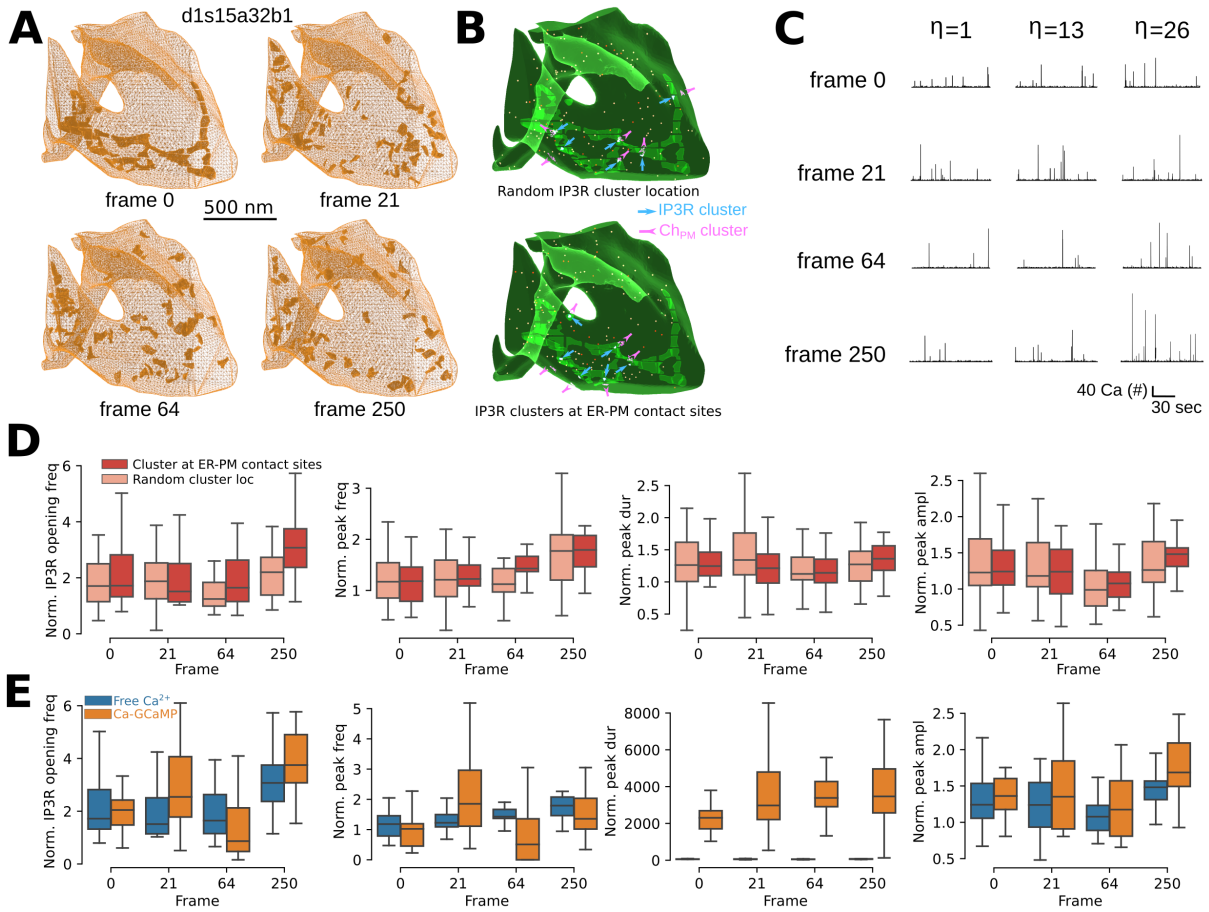


Fig 9: Ca^{2+} buffering and IP_3R channel location mediate the effect of ER-PM distance on Ca^{2+} microdomain activity in PAPs. (A) Images presenting different meshes created from PAP d1s15a32b1 using the automated workflow presented in Fig. 8: frames 0, 21, 64 and 250, characterized by diverse ER distributions within the PAP with constant PAP and ER shape, volume and surface area. Characteristics of ER-PM distance in those meshes are displayed in Fig. 8B-D. (B) Screenshots of simulations performed in d1s15a32b1_{f0} mesh (frame 0), with IP_3R clusters (blue, arrows) distributed randomly on the ER membrane (top) or at ER-PM contact sites (bottom). IP_3R clusters were co-localized with Ch_{PM} clusters at the plasma membrane (purple, inverse arrows): $cocl=1$. (C) Representative free Ca^{2+} traces in frames 0, 21, 64 and 250, with IP_3R cluster size $\eta=1$, 13 and 26 and random distribution of IP_3R clusters on the ER. (D) Quantification of IP_3R opening frequency (left), Ca^{2+} peak frequency (middle left), duration (middle right) and amplitude (right), in frames 0, 21, 64 and 250, for $\eta=26$, normalized by Ca^{2+} peak characteristics for $\eta=1$ in each mesh, with IP_3R clusters at random locations on the ER (left, light red) or at ER-PM contact sites (right, dark red).

Fig 9: (E) Quantification of IP₃R opening frequency (left), peak frequency (middle left), duration (middle right) and amplitude (right) of free Ca²⁺ signals (blue) and Ca-GCaMP signals (orange), in frames 0, 21, 64 and 250, for $\eta=26$, normalized by Ca²⁺ peak characteristics for $\eta=1$. IP₃R clusters were located at ER-PM contact sites. n=20 for each parameter set tested.

Discussion

Here, we extracted 3D meshes of tripartite synapses from a 220 μm^3 hippocampal astrocytic volume from the CA1 stratum radiatum region, reconstructed from EM (47). Quantification of the geometrical features of those meshes highlighted the diverse geometrical properties of PAPs from a single astrocyte and revealed, contrary to a widespread belief that PAPs are devoid of ER (23, 44), that 75 % of PAPs contained some ER. Interestingly, we found that PAPs are the closest to the synapse when bouton surface area is low, which could result from the spatial constraints imposed by larger boutons, preventing the PAP from getting in close contact to the PSD. Reaction-diffusion simulations in the realistic PAP 3D meshes reconstructed in this study provided key insights into the effect of the diverse shapes and distributions of the ER in PAPs on microdomain Ca²⁺ activity. As reactive astrocytes, hallmark of brain diseases (62), are characterized by a remodelling of ER volume and shape (63), our results suggest that such geometrical alterations of the ER could be one of the factors responsible for the altered astrocytic Ca²⁺ activity reported in pathological conditions (64).

Fine-tuning the spatial distribution of Ca²⁺ channels, monitoring channel opening events at each channel, while independently manipulating ER shape and distribution, such as performed in this study, is not feasible experimentally. It is yet essential to understand the mechanistic link between the spatial features of the astrocyte and its Ca²⁺ microdomain activity. Combining our detailed biophysical model of Ca²⁺ signals in PAPs, the PAP meshes that we extracted from EM and the realistic PAP meshes with various ER distributions generated by our automated mesh generator allowed us to provide key insights into Ca²⁺ signaling in PAPs. Notably, we predict how the complex interplay between the clustering of Ca²⁺ channels, the ratio between ER surface area and PAP volume, Ca²⁺ buffering and the size and location of ER-PM contact sites shapes Ca²⁺ microdomain signals at tripartite synapses. This study is the first to our knowledge to model Ca²⁺ activity in astrocytes with realistic shapes in 3D at the nanoscale that accounts for the complex and diverse spatial characteristics of Ca²⁺ stores in PAPs. Furthermore, our results highlight the impact of the modeling choices on simulation results, notably when investigating spatial effects. Importantly, our results nuance the effect of the clustering of Ca²⁺ channels, which is stronger in 2D or simple 3D shapes than in more realistic 3D meshes. This is crucial as, until now, modeling studies on PAPs were conducted in 1D, 2D or in simple 3D shapes, notably cylinders (49, 65–69). The 3D meshes provided by this study, together with our realistic 3D PAP mesh generator, pave the way for future modeling studies in realistic 3D meshes to investigate the mechanisms governing neuron-astrocyte communication at tripartite

364 synapses.

365

366 The geometrical data used here were extracted from electron microscopy, which is the only
367 tool that can resolve PAP and ER shape at a high spatial resolution (6 nm here), yet results
368 in potential alterations of the ultrastructure of the extracellular space (70) and cannot be used
369 to study live cells. Furthermore, the model used in this study, focusing on the effect of the
370 ER shape and distribution on Ca^{2+} activity, describes with great details the kinetics of ER-
371 mediated Ca^{2+} signals while simplifying other Ca^{2+} sources. Other Ca^{2+} sources and chan-
372 nels however contribute to Ca^{2+} microdomain activity in PAPs, including mitochondria, the
373 $\text{Na}^+/\text{Ca}^{2+}$ exchanger, transient receptor potential ankyrin 1 channels, L-type voltage gated
374 channels and other pathways (27, 43). According to our model's predictions, the spatial dis-
375 tribution of Ca^{2+} channels can alter the spatio-temporal properties of Ca^{2+} microdomain sig-
376 nals in PAPs as well as their amplification upon neuronal stimulation. Further quantification
377 of the Ca^{2+} channels expressed in PAPs, their density, location and remodeling in live tissue
378 under (patho-)physiological conditions is thus essential to better understand astrocyte activity
379 at synapses. The recent advances in super-resolution techniques, notably single particle track-
380 ing methods, provide a promising avenue to overcome current limitations in obtaining such
381 data (21, 71).

382

383 Recent super-resolution studies in live neurons revealed dynamical remodeling of ER-PM
384 contact sites (72) and diffusional trapping of molecules resulting from the ER remodeling (73)
385 in neurons. Those observations, together with our model predictions, highlight the need for fur-
386 ther quantification of the dynamical shape and distribution of the ER in astrocytes in live tissue
387 to fully grasp its influence on Ca^{2+} microdomain activity in astrocytes. According to our model
388 predictions, preferential location of IP_3Rs at ER-PM contact sites might be essential to allow
389 signal amplification with IP_3R cluster size and could thus strongly alter the spatio-temporal
390 properties of astrocytic Ca^{2+} signals evoked by neurotransmitters, potentially affecting the sub-
391 sequent modulation of neuronal activity by astrocytes. Our results, in accordance with previous
392 computational studies in other cell types (52), highlight that Ca^{2+} buffering plays a crucial role
393 in shaping Ca^{2+} activity at ER-PM contact sites. The Ca^{2+} buffering effect described here was
394 mediated by Ca^{2+} indicators. Future experimental and computational studies will be essential
395 to assess Ca^{2+} buffering mechanisms in astrocytes and PAPs, which are still poorly understood,
396 yet, according to our simulation results, play crucial roles in shaping Ca^{2+} microdomain activ-
397 ity in astrocytes.

398

399 Overall, this study provides new insights into astrocytic activity at tripartite synapses by
400 characterizing the presence, shape and distribution of the ER in PAPs and by shedding light
401 to the mechanistic link between those features and microdomain Ca^{2+} activity at tripartite
402 synapses. The realistic 3D meshes of tripartite synapses created in this study pave the way for
403 new modeling studies of neuron-astrocyte communication in the synaptic micro-environment,
404 allowing the study of various processes, such as glutamate spillover or gliotransmission. Such

405 studies will be crucial to decipher whether the various nano-architectures displayed by tripartite
406 synapses reflect distinct functional identities.

407 **Materials and Methods**

408 **3D reconstruction from electron microscopy**

409 **Sample preparation and imaging**

410 The original dataset used in this work (EM stack and 3D reconstructions) was previously pub-
411 lished in (47). The block was a gift from Graham Knott (BioEM imaging facility at EPFL,
412 Lausanne, Switzerland). All procedures were performed according to the Swiss Federal Laws.
413 One P90 Sprague-Dawley rat was deeply anesthetized with isoflurane and transcardially per-
414 fused using 2% paraformaldehyde and 2.5% glutaraldehyde in PBS 0.1M. Coronal sections
415 ($100\ \mu\text{m}$) were obtained and washed in cacodylate buffer, followed by a post-fixation using
416 osmium tetroxide and uranyl acetate. Finally, the sections were embedded in Durcupan. Re-
417 gions of the hippocampus were dissected under a stereoscopic microscope, mounted onto a
418 blank resin slab, and trimmed using an ultramicrotome (Laica Ultracut UC-7). Imaging was
419 performed using an NVision 40 FIB-SEM (Carl Zeiss) with an acceleration voltage of 1.5 kV, a
420 current of 350 pA, and a dwell time of $10\ \mu\text{s}/\text{pixel}$. Serial images were obtained using backscat-
421 tered electrons and collected at a 6 nm/pixel magnification and 5 nm of milling depth between
422 images.

423 **3D reconstruction and rendering**

424 The serial micrographs were first registered using Multistackreg, a freely available plug-in
425 for Fiji (47). Then, using those micrographs, we proceeded to the image segmentation and
426 3D model reconstructions by using TrackEM2 (a plug-in for Fiji) for manual segmentation,
427 and iLastik, for a semi-automated segmentation. The extracted models were then imported to
428 Blender software for visualization and rendering purposes (74).

429 **Extraction of tripartite synapse meshes**

430 For each synapse in contact with the $220\ \mu\text{m}^3$ astrocytic volume, a cube of edge length $1.5\ \mu\text{m}$
431 ($3.375\ \mu\text{m}^3$) was created and centered at the center of mass of the PSD. All the elements of
432 the mesh (astrocyte, astrocytic ER, spine and bouton) that were within the cubic volume were
433 isolated using a boolean intersection operator available in Blender, forming what we refer to
434 as a tripartite synapse mesh. The size of the cube was chosen to contain a single synapse (the
435 neuropil is believed to contain around one synapse per micrometer cube) and large enough to
436 contain the whole spine and bouton elements. This workflow resulted in the creation of 44
437 excitatory and 2 inhibitory synapse meshes.

438 **Computational modeling**

439 **Modeled reactions and computational approach**

440 Astrocytic Ca^{2+} signals in PAPs were simulated using the reaction-diffusion voxel-based model
441 of ER-dependent Ca^{2+} signaling from Denizot and colleagues ((49) Table 2, Fig. 6-7). Briefly,
442 the model describes Ca^{2+} fluxes in and out of the astrocytic cytosol. The opening of IP_3R chan-
443 nels on the ER membrane triggers Ca^{2+} influx in the cytosol. IP_3 can be synthesized by the
444 Ca^{2+} -dependent activity of Phospholipase C (PLC) δ . IP_3 removal from the cytosol is described
445 by a decay rate. IP_3R dynamics is derived from the De Young & Keizer’s model (75). Each
446 IP_3R has 3 binding sites: one to IP_3 and two to Ca^{2+} (activating and inhibiting). The channel
447 can thus be in 8 different states. The open state is $\{110\}$: IP_3 and Ca^{2+} bound to the acti-
448 vating sites and the Ca^{2+} inactivating site is unbound. In a subset of simulations, GCaMPs6s,
449 genetically-encoded Ca^{2+} indicators (27), were added to the cytosol and variations of $[\text{Ca-}$
450 $\text{GCaMP}]$ concentration, mimicking experimental Ca^{2+} imaging, were measured. For further
451 details on the kinetic scheme, parameter values and model assumptions, please refer to the
452 original paper presenting the model (49). We slightly altered this model to better describe and
453 control IP_3R -independent Ca^{2+} fluxes. To do so, IP_3R -independent Ca^{2+} influx was modeled
454 as an influx through Ca^{2+} channels at the plasma membrane, Ch_{PM} . For simplicity, the amount
455 of Ch_{PM} channels equals the total number of IP_3R channels, $N_{\text{IP}_3\text{R}}$. Ca^{2+} influx rate at Ch_{PM}
456 channels, $\gamma_{\text{ch}_{\text{PM}}}$, is $15 \times 10^{-8} \text{s}^{-1}$. The reactions modeled here are illustrated in Fig. 4A.

457
458 The model was implemented using the STochastic Engine for Pathway Simulation (STEPS)
459 python package (<http://steps.sourceforge.net/>) (76). This software uses a spatialized version of
460 Gillespie’s SSA algorithm (77) to perform exact stochastic simulations of reaction-diffusion
461 systems. Simulations in STEPS allow the diffusion of molecules in 3D tetrahedral meshes and
462 onto the surfaces of the mesh, such as the ER and plasma membrane. STEPS allows volume
463 and surface reactions. Reactions can only occur between molecules within the same tetrahe-
464 dron (volume reactions) or in adjacent triangle and tetrahedron (surface reactions). Boundary
465 conditions were reflective. Simulation time was 100s. The states and amounts of all molecular
466 species were measured at each time step (1 ms).

467 **Neuronal stimulation simulation**

468 Unless specified otherwise, glutamatergic transmission at the synapse was modeled and oc-
469 curred at simulation time $t=1\text{s}$. To do so, IP_3 molecules were injected in tetrahedra below
470 the plasma membrane of the PAP, emulating IP_3 synthesis resulting from the activation of
471 metabotropic glutamatergic receptors at the membrane of the PAP. Supplemental movie 3 presents
472 a visualization of a simulation at neuronal stimulation time, in the d2s6a9b1 PAP mesh.

473 Ca^{2+} channel clustering algorithm

474 Surfaces correspond to triangular meshes. To simulate IP_3R clustering, $N_{\text{IP}_3\text{R}}/\eta$ IP_3R clusters
475 were randomly positioned onto the membrane of the ER, where $N_{\text{IP}_3\text{R}}$ is the total number of
476 IP_3Rs and η is the number of channels per cluster. As η is an integer, it must be a divider
477 of $N_{\text{IP}_3\text{R}}$. As IP_3R density was kept constant across simulations, $3.5e^{-3}/\mu\text{m}^2$ (49), the total
478 number of IP_3Rs , $N_{\text{IP}_3\text{R}}$, and IP_3R cluster size η varied depending on the mesh. Each IP_3R
479 cluster was located within a region of interest, as defined in STEPS, consisting in 4 triangles.
480 Clusters could not overlap. In a subset of simulations, IP_3R clusters were located at ER-PM
481 contact sites. To do so, ER triangles were sorted depending on the distance between their center
482 of mass and the closest PM triangle. Cluster center was then located at the ER triangle in which
483 no cluster was already located characterized by the lowest ER-PM distance in the mesh. The
484 cluster ROI consisted in this cluster center triangle and the neighboring triangles. Similarly,
485 clusters could not overlap. The number of IP_3R opening events at each cluster ROI was mea-
486 sured at each time step.

487

488 IP_3R channels were co-clustered with Ch_{PM} Ca^{2+} channels at the plasma membrane ($\text{cocl}=1$),
489 unless specified otherwise. If $\text{cocl}=0$, Ch_{PM} channels were randomly distributed onto the
490 plasma membrane. If $\text{cocl}=1$, Ch_{PM} channels were co-clustered with IP_3Rs . To do so, Ch_{PM}
491 cluster center was defined as the triangle on the plasma membrane that was the closest to the
492 IP_3R cluster center triangle on the ER. The cluster ROI then consisted in this Ch_{PM} cluster
493 center and the neighboring triangles. Similarly to IP_3R cluster ROIs, Ch_{PM} clusters could not
494 overlap. For simplicity, Ch_{PM} cluster size was identical to IP_3R cluster size: η .

495 Simulation code

496 Simulations were performed using the model of Ca^{2+} signals in fine processes from Denizot
497 and collaborators (49), available at <http://modeldb.yale.edu/247694>.

498 Ca^{2+} peak detection and characterization

499 Ca^{2+} peaks were considered initiated and terminated when Ca^{2+} concentration increased above
500 and decreased below peak threshold, respectively. Peak threshold was $[Ca]_b + n\sigma_{\text{Ca}}$, where
501 $[Ca]_b$ is the basal Ca^{2+} concentration and σ_{Ca} is the standard deviation of the $[\text{Ca}^{2+}]$ histogram
502 in the absence of neuronal stimulation. n varied depending on signal/noise ratio of the simula-
503 tion of interest, notably when measuring Ca-GCaMP signals, noisier than free Ca^{2+} signals (see
504 (e.g.) Fig 4E). Ca^{2+} peak frequency, duration and amplitude were measured in each simulation.
505 Ca^{2+} peak duration corresponds to the time between peak initiation and termination, Ca^{2+} peak
506 amplitude corresponds to the maximum number of Ca^{2+} ions in the cytosol measured within
507 peak duration time and Ca^{2+} peak frequency corresponds to the amount of peaks detected dur-
508 ing simulation time. The number of IP_3R peak opening events was recorded at each time step,
509 in the whole cell as well as at each IP_3R cluster ROI.

510 **3D mesh manipulation**

511 All 3D mesh manipulations were performed with open-access, open-source software. All PAP
512 3D meshes used in this study will be available online upon paper acceptance.

513 **3D PAP mesh processing for reaction-diffusion simulations**

514 PAP meshes from tripartite synapse meshes were pre-processed using Blender software so that
515 they could be used for reaction-diffusion simulations. The workflow is illustrated in Fig. 4C.
516 Intersection between ER and PAP membranes was prevented by using a boolean intersection
517 operator. ER was relocated a few nanometers away from the plasma membrane. PAP compart-
518 ments that did not belong to the main PAP volume were deleted. Boolean difference operation
519 between PAP and ER elements was performed. Non-manifold vertices were repaired. The
520 resulting PAP mesh was exported in .stl format, which was then converted into a .msh 3D tetra-
521 hedral mesh using TetWild software (78). Lastly, the mesh was imported into Gmsh software
522 to be converted into 2.2 ASCII format, format supported by the STEPS mesh importer.

523 **Automated 3D PAP mesh generation**

524 We have implemented a workflow to generate realistic 3D tetrahedral PAP meshes characterized
525 by various ER locations and constant ER shape. The algorithm is written in python, can be
526 imported in Blender and will be available online upon paper acceptance. The workflow is
527 presented in Fig. 8. First, all elements of the mesh, i.e the PAP and the ER, are relocated
528 so that their center of mass is centered at the origin. Then, the ER is split into smaller ER
529 objects using a custom-made function. Briefly, n cubes of a given size are placed along the
530 ER object. Intersection boolean operation is then performed between the ER and each cube,
531 resulting in the creation of n ER objects. ER objects smaller than 30 nm^3 are deleted. The
532 remaining ER objects are rescaled so that the sum of their surface areas matches the area of
533 the original ER element, measured with the Blender 3D Print add-on. The number and size of
534 cubes can be altered depending on the size of the original ER and on the mesh characteristics
535 desired. Using Blender's physics engine, a simulation with n frames is generated, in which ER
536 objects are subject to physical forces that alter their location between each frame. Inputs of the
537 'RunPhysics' function include parameters that affect how close objects can get, which can be
538 altered to prevent membrane intersection. Note that successful scattering of the ER depends on
539 the geometrical properties of each mesh so that adjusting the parameters of physics simulation
540 might be necessary depending on the mesh used. Details are provided in comments of the code
541 to allow the user to adjust the code to the mesh under study. Examples of frames generated by
542 this workflow applied to d1s15a32b1 PAP mesh is presented in Supplemental movie 2. For each
543 selected frame, the mesh pre-processing steps presented in Fig. 4C are performed automatically,
544 resulting in the export of a .stl triangular mesh. 3D meshing and format conversion can then be
545 performed using TetWild and Gmsh software, as described above. The resulting meshes can be
546 used to perform reaction-diffusion simulations.

547 **Analysis of the geometrical properties of 3D meshes**

548 The volume and surface area of each synaptic element, i.e the PAP, astrocytic ER, spine and
549 bouton, were measured using the Blender add-on Neuromorph (79). We implemented a python
550 script that can be imported in Blender software that measures distances between mesh elements
551 of interest. The distance between each vertex of the plasma membrane of the PAP and the
552 center of mass of the neighboring PSD was computed in Blender and stored in a list. Similarly,
553 ER-PSD distance was quantified by measuring the distance between each vertex of the ER
554 membrane and the center of mass of the PSD. To characterize ER-PM distance, for each vertex
555 on the PM, the closest ER vertex was detected and its distance to the PM vertex was stored in
556 a list. PM-PSD, ER-PSD and ER-PM distance lists were exported to a text file for analysis and
557 visualisation.

558 **Statistical analysis**

559 Data analysis and statistics were performed using open-access and open-source software: the
560 SciPy and pandas python libraries. Data visualization was performed using Seaborn and Mat-
561 plotlib python libraries. Sample size for each analysis, n , is described in the figure legend.
562 Prior to statistical analysis, normality of data distribution was inferred using the Shapiro-Wilk
563 test. Relationship between Ca^{2+} peak characteristics and parameter values was inferred using
564 one-way ANOVA if values followed a Gaussian distribution, Kruskal-Wallis one-way ANOVA
565 otherwise. Note that the effect of IP_3R clustering was quantified by measuring the ratio be-
566 tween the Ca^{2+} peak characteristic of interest measured at a given IP_3R cluster size, $\eta > 1$
567 and its mean value for $\eta=1$. The linear relationship between two datasets was evaluated using
568 Spearman's correlation coefficient. The test and p-value, p , associated with each analysis is
569 described in the figure legend or in the main text.

570 **References**

- 571 1. A. Verkhratsky, M. Nedergaard, Physiology of Astroglia. *Physiological Reviews* **98**, 239–
572 389 (2018).
- 573 2. A. Araque, V. Parpura, R. P. Sanzgiri, P. G. Haydon, Tripartite synapses: glia, the unac-
574 knowledged partner. *Trends in Neurosciences* **22**, 208–215 (1999).
- 575 3. I. Savtchouk, A. Volterra, Gliotransmission: Beyond Black-and-White. *Journal of Neuro-*
576 *science* **38**, 14–25 (2018).
- 577 4. E. A. Bushong, M. E. Martone, Y. Z. Jones, M. H. Ellisman, Protoplasmic astrocytes in
578 CA1 stratum radiatum occupy separate anatomical domains. *The Journal of Neuroscience:*
579 *The Official Journal of the Society for Neuroscience* **22**, 183–192 (2002).

- 580 5. M. R. Witcher, S. A. Kirov, K. M. Harris, Plasticity of perisynaptic astroglia during synap-
581 togenesis in the mature rat hippocampus. *Glia* **55**, 13–23 (2007).
- 582 6. I. Lushnikova, G. Skibo, D. Muller, I. Nikonenko, Synaptic potentiation induces increased
583 glial coverage of excitatory synapses in CA1 hippocampus. *Hippocampus* **19**, 753–762
584 (2009).
- 585 7. M. K. Herde, K. Bohmbach, C. Domingos, N. Vana, J. A. Komorowska-Müller, S. Passlick,
586 I. Schwarz, C. J. Jackson, D. Dietrich, M. K. Schwarz, C. Henneberger, Local Efficacy of
587 Glutamate Uptake Decreases with Synapse Size. *Cell Reports* **32**, 108182 (2020).
- 588 8. C. Henneberger, L. Bard, A. Panatier, J. P. Reynolds, O. Kopach, N. I. Medvedev, D. Minge,
589 M. K. Herde, S. Anders, I. Kraev, J. P. Heller, S. Rama, K. Zheng, T. P. Jensen, I. Sanchez-
590 Romero, C. J. Jackson, H. Janovjak, O. P. Ottersen, E. A. Nagelhus, S. H. R. Oliet, M. G.
591 Stewart, U. V. Nägerl, D. A. Rusakov, LTP Induction Boosts Glutamate Spillover by Driv-
592 ing Withdrawal of Perisynaptic Astroglia. *Neuron* (2020).
- 593 9. A. Badia-Soteras, T. S. Heistek, M. Kater, A. Negrean, H. S. Mansvelder, B. Khakh, R. Min,
594 A. Smit, M. Verheijen, Proximity of astrocyte leaflets to the synapse determines memory
595 strength, *Tech. rep.*, bioRxiv (2022). Section: New Results Type: article.
- 596 10. A. Reichenbach, A. Derouiche, F. Kirchhoff, Morphology and dynamics of perisynaptic
597 glia. *Brain Research Reviews* **63**, 11–25 (2010).
- 598 11. Y. Bernardinelli, J. Randall, E. Janett, I. Nikonenko, S. König, E. V. Jones, C. E. Flores,
599 K. K. Murai, C. G. Bochet, A. Holtmaat, D. Muller, Activity-dependent structural plasticity
600 of perisynaptic astrocytic domains promotes excitatory synapse stability. *Current biology:*
601 *CB* **24**, 1679–1688 (2014).
- 602 12. A. Verkhratsky, M. Nedergaard, Astroglial cradle in the life of the synapse. *Philosophical*
603 *Transactions of the Royal Society B: Biological Sciences* **369** (2014).
- 604 13. A. Araque, G. Carmignoto, P. G. Haydon, S. H. R. Oliet, R. Robitaille, A. Volterra, Glio-
605 transmitters travel in time and space. *Neuron* **81**, 728–739 (2014).
- 606 14. N. Mazaré, M. Oudart, J. Moulard, G. Cheung, R. Tortuyaux, P. Mailly, D. Mazaud, A.-P.
607 Bemelmans, A.-C. Boulay, C. Blugeon, L. Jourden, S. Le Crom, N. Rouach, M. Cohen-
608 Salmon, Local Translation in Perisynaptic Astrocytic Processes Is Specific and Changes
609 after Fear Conditioning. *Cell Reports* **32**, 108076 (2020).
- 610 15. J. B. Foster, F. Zhao, X. Wang, Z. Xu, K. Lin, C. C. Askwith, K. J. Hodgetts, C.-L.
611 Glenn Lin, Pyridazine-derivatives enhance structural and functional plasticity of tripartite
612 synapse via activation of local translation in astrocytic processes. *Neuroscience* (2018).

- 613 16. L. E. Ostroff, M. K. Manzur, C. K. Cain, J. E. LeDoux, Synapses lacking astrocyte appear
614 in the amygdala during consolidation of Pavlovian threat conditioning. *The Journal of*
615 *comparative neurology* **522**, 2152–2163 (2014).
- 616 17. A. Panatier, D. T. Theodosis, J.-P. Mothet, B. Touquet, L. Pollegioni, D. A. Poulain, S. H. R.
617 Oliet, Glia-Derived d-Serine Controls NMDA Receptor Activity and Synaptic Memory.
618 *Cell* **125**, 775–784 (2006).
- 619 18. A. Perez-Alvarez, M. Navarrete, A. Covelo, E. D. Martin, A. Araque, Structural and func-
620 tional plasticity of astrocyte processes and dendritic spine interactions. *The Journal of Neu-*
621 *roscience: The Official Journal of the Society for Neuroscience* **34**, 12738–12744 (2014).
- 622 19. C. Genoud, C. Quairiaux, P. Steiner, H. Hirling, E. Welker, G. W. Knott, Plasticity of
623 Astrocytic Coverage and Glutamate Transporter Expression in Adult Mouse Cortex. *PLoS*
624 *Biology* **4**, e343 (2006).
- 625 20. J. Wenzel, G. Lammert, U. Meyer, M. Krug, The influence of long-term potentiation on
626 the spatial relationship between astrocyte processes and potentiated synapses in the dentate
627 gyrus neuropil of rat brain. *Brain Research* **560**, 122–131 (1991).
- 628 21. J. P. Heller, D. A. Rusakov, The Nanoworld of the Tripartite Synapse: Insights from Super-
629 Resolution Microscopy. *Frontiers in Cellular Neuroscience* **11** (2017).
- 630 22. M. Arizono, V. V. G. K. Inavalli, S. Bancelin, M. Fernández-Monreal, U. V. Nägerl,
631 Super-resolution shadow imaging reveals local remodeling of astrocytic microstructures
632 and brain extracellular space after osmotic challenge. *Glia* **69**, 1605–1613 (2021). eprint:
633 <https://onlinelibrary.wiley.com/doi/pdf/10.1002/glia.23995>.
- 634 23. D. A. Rusakov, Disentangling calcium-driven astrocyte physiology. *Nature Reviews Neu-*
635 *roscience* **16**, 226–233 (2015).
- 636 24. A. Aboufares El Alaoui, M. Jackson, M. Fabri, L. de Vivo, M. Bellesi, Characterization
637 of Subcellular Organelles in Cortical Perisynaptic Astrocytes. *Frontiers in Cellular Neuro-*
638 *science* **14** (2021). Publisher: Frontiers.
- 639 25. A. Verkhratsky, A. Semyanov, R. Zorec, Physiology of Astroglial Excitability. *Function* **1**
640 (2020).
- 641 26. A. Semyanov, C. Henneberger, A. Agarwal, Making sense of astrocytic calcium signals
642 — from acquisition to interpretation. *Nature Reviews Neuroscience* pp. 1–14 (2020). Pub-
643 lisher: Nature Publishing Group.
- 644 27. E. Shigetomi, S. Patel, B. S. Khakh, Probing the Complexities of Astrocyte Calcium Sig-
645 naling. *Trends in Cell Biology* **26**, 300–312 (2016).

- 646 28. A. Lia, V. J. Henriques, M. Zonta, A. Chiavegato, G. Carmignoto, M. Gómez-Gonzalo,
647 G. Losi, Calcium Signals in Astrocyte Microdomains, a Decade of Great Advances. *Frontiers in Cellular Neuroscience* **15** (2021). Publisher: Frontiers.
648
- 649 29. L. Georgiou, A. Echeverría, A. Georgiou, B. Kuhn, Ca⁺ activity maps of astrocytes tagged
650 by axoastrocytic AAV transfer. *Science Advances* **8**, eabe5371 (2022). Publisher: American
651 Association for the Advancement of Science.
- 652 30. A. Agarwal, P.-H. Wu, E. G. Hughes, M. Fukaya, M. A. Tischfield, A. J. Langseth, D. Wirtz,
653 D. E. Bergles, Transient Opening of the Mitochondrial Permeability Transition Pore In-
654 duces Microdomain Calcium Transients in Astrocyte Processes. *Neuron* **93**, 587–605.e7
655 (2017).
- 656 31. E. Bindocci, I. Savtchouk, N. Liaudet, D. Becker, G. Carriero, A. Volterra, Three-
657 dimensional Ca²⁺ imaging advances understanding of astrocyte biology. *Science* **356**,
658 eaai8185 (2017).
- 659 32. A. Asada, S. Ujita, R. Nakayama, S. Oba, S. Ishii, N. Matsuki, Y. Ikegaya, Subtle modula-
660 tion of ongoing calcium dynamics in astrocytic microdomains by sensory inputs. *Physio-
661 logical Reports* **3** (2015).
- 662 33. E. Shigetomi, E. A. Bushong, M. D. Haustein, X. Tong, O. Jackson-Weaver, S. Kracun,
663 J. Xu, M. V. Sofroniew, M. H. Ellisman, B. S. Khakh, Imaging calcium microdomains
664 within entire astrocyte territories and endfeet with GCaMPs expressed using adeno-
665 associated viruses. *The Journal of General Physiology* **141**, 633–647 (2013).
- 666 34. M.-Y. Sun, P. Devaraju, A. X. Xie, I. Holman, E. Samones, T. R. Murphy, T. A. Fiacco,
667 Astrocyte calcium microdomains are inhibited by Bafilomycin A1 and cannot be replicated
668 by low-level Schaffer collateral stimulation in situ. *Cell Calcium* **55**, 1–16 (2014).
- 669 35. J. L. Stobart, K. D. Ferrari, M. J. P. Barrett, C. Glück, M. J. Stobart, M. Zuend, B. Weber,
670 Cortical Circuit Activity Evokes Rapid Astrocyte Calcium Signals on a Similar Timescale
671 to Neurons. *Neuron* **98**, 726–735.e4 (2018).
- 672 36. R. Srinivasan, B. S. Huang, S. Venugopal, A. D. Johnston, H. Chai, H. Zeng, P. Golshani,
673 B. S. Khakh, Ca(2+) signaling in astrocytes from Ip3r2(-/-) mice in brain slices and during
674 startle responses in vivo. *Nature Neuroscience* **18**, 708–717 (2015).
- 675 37. M. W. Sherwood, M. Arizono, C. Hisatsune, H. Bannai, E. Ebisui, J. L. Sherwood, A. Pa-
676 natier, S. H. R. Oliet, K. Mikoshiba, Astrocytic IP3Rs: Contribution to Ca²⁺ signalling and
677 hippocampal LTP. *Glia* **65**, 502–513 (2017).
- 678 38. A. Panatier, J. Vallée, M. Haber, K. K. Murai, J.-C. Lacaille, R. Robitaille, Astrocytes are
679 endogenous regulators of basal transmission at central synapses. *Cell* **146**, 785–798 (2011).

- 680 39. M. A. Di Castro, J. Chuquet, N. Liaudet, K. Bhaukaurally, M. Santello, D. Bouvier, P. Tiret,
681 A. Volterra, Local Ca²⁺ detection and modulation of synaptic release by astrocytes. *Nature*
682 *Neuroscience* **14**, 1276–1284 (2011).
- 683 40. B. L. Lind, A. R. Brazhe, S. B. Jessen, F. C. C. Tan, M. J. Lauritzen, Rapid stimulus-evoked
684 astrocyte Ca²⁺ elevations and hemodynamic responses in mouse somatosensory cortex in
685 vivo. *Proceedings of the National Academy of Sciences* p. 201310065 (2013).
- 686 41. A. Panatier, M. Arizono, U. V. Nägerl, Dissecting tripartite synapses with STED mi-
687 croscopy. *Phil. Trans. R. Soc. B* **369**, 20130597 (2014).
- 688 42. M. Arizono, V. V. G. K. Inavalli, A. Panatier, T. Pfeiffer, J. Angibaud, F. Levet, M. J. T. T.
689 Veer, J. Stobart, L. Bellocchio, K. Mikoshiba, G. Marsicano, B. Weber, S. H. R. Oliet,
690 U. V. Nägerl, Structural basis of astrocytic Ca²⁺ signals at tripartite synapses. *Nature*
691 *Communications* **11**, 1–15 (2020). Number: 1 Publisher: Nature Publishing Group.
- 692 43. M. W. Sherwood, M. Arizono, A. Panatier, K. Mikoshiba, S. H. R. Oliet, Astrocytic IP3Rs:
693 Beyond IP3R2. *Frontiers in Cellular Neuroscience* **0** (2021). Publisher: Frontiers.
- 694 44. I. Patrushev, N. Gavrilov, V. Turlapov, A. Semyanov, Subcellular location of astrocytic
695 calcium stores favors extrasynaptic neuron-astrocyte communication. *Cell Calcium* **54**,
696 343–349 (2013).
- 697 45. C. M. Kiyoshi, S. Aten, E. P. Arzola, J. A. Patterson, A. T. Taylor, Y. Du, A. M. Guiher,
698 M. Philip, E. G. Camacho, D. Mediratta, K. Collins, E. Benson, G. Kidd, D. Terman,
699 M. Zhou, Ultrastructural view of astrocyte-astrocyte and astrocyte-synapse contacts within
700 the hippocampus. *bioRxiv* p. 2020.10.28.358200 (2020). Publisher: Cold Spring Harbor
701 Laboratory Section: New Results.
- 702 46. L. H. Bergersen, C. Morland, L. Ormel, J. E. Rinholm, M. Larsson, J. F. H. Wold, A. T.
703 Roe, A. Stranna, M. Santello, D. Bouvier, O. P. Ottersen, A. Volterra, V. Gundersen, Im-
704 munogold Detection of L-glutamate and D-serine in Small Synaptic-Like Microvesicles in
705 Adult Hippocampal Astrocytes. *Cerebral Cortex* **22**, 1690–1697 (2012).
- 706 47. C. Cali, J. Baghabra, D. J. Boges, G. R. Holst, A. Kreshuk, F. A. Hamprecht, M. Srinivasan,
707 H. Lehväslaiho, P. J. Magistretti, Three-dimensional immersive virtual reality for studying
708 cellular compartments in 3D models from EM preparations of neural tissues. *Journal of*
709 *Comparative Neurology* **524**, 23–38 (2016).
- 710 48. N. Medvedev, V. Popov, C. Henneberger, I. Kraev, D. A. Rusakov, M. G. Stewart, Glia
711 selectively approach synapses on thin dendritic spines. *Phil. Trans. R. Soc. B* **369**, 20140047
712 (2014).

- 713 49. A. Denizot, M. Arizono, U. V. Nägerl, H. Soula, H. Berry, Simulation of calcium signaling
714 in fine astrocytic processes: Effect of spatial properties on spontaneous activity. *PLOS*
715 *Computational Biology* **15**, e1006795 (2019).
- 716 50. I. Hepburn, R. Cannon, E. De Schutter, Efficient calculation of the quasi-static electrical po-
717 tential on a tetrahedral mesh and its implementation in STEPS. *Frontiers in Computational*
718 *Neuroscience* **7** (2013).
- 719 51. A. Denizot, M. Arizono, U. V. Nägerl, H. Soula, H. Berry, Spontaneous astrocytic calcium
720 traces from organotypic hippocampal slices (2019). Publisher: figshare Type: dataset.
- 721 52. S. Zeller, S. Rüdiger, H. Engel, J. Sneyd, G. Warnecke, I. Parker, M. Falcke, Modeling of
722 the modulation by buffers of Ca²⁺ release through clusters of IP₃ receptors. *Biophysical*
723 *Journal* **97**, 992–1002 (2009).
- 724 53. S. M. Wiltgen, I. F. Smith, I. Parker, Superresolution localization of single functional IP₃R
725 channels utilizing Ca²⁺ flux as a readout. *Biophysical Journal* **99**, 437–446 (2010).
- 726 54. N. B. Thillaiappan, A. Chavda, S. Tovey, D. Prole, C. Taylor, Ca²⁺ signals initiate at im-
727 mobile IP₃ receptors adjacent to ER-plasma membrane junctions. *Nature Communications*
728 **8** (2017).
- 729 55. Taufiq-Ur-Rahman, A. Skupin, M. Falcke, C. W. Taylor, Clustering of InsP₃ receptors by
730 InsP₃ retunes their regulation by InsP₃ and Ca²⁺. *Nature* **458**, 655–659 (2009).
- 731 56. I. F. Smith, S. M. Wiltgen, J. Shuai, I. Parker, Ca²⁺ Puffs Originate from Prestablished
732 Stable Clusters of Inositol Trisphosphate Receptors. *Sci. Signal.* **2**, ra77–ra77 (2009).
- 733 57. S. Rüdiger, J. Shuai, Modeling of Stochastic Ca²⁺ Signals. *Computational Glioscience*,
734 M. De Pittà, H. Berry, eds., Springer Series in Computational Neuroscience (Springer In-
735 ternational Publishing, Cham, 2019), pp. 91–114.
- 736 58. L. Lencesova, A. O’Neill, W. G. Resneck, R. J. Bloch, M. P. Blaustein, Plasma membrane-
737 cytoskeleton-endoplasmic reticulum complexes in neurons and astrocytes. *The Journal of*
738 *Biological Chemistry* **279**, 2885–2893 (2004).
- 739 59. A. Denizot, H. Berry, S. Venugopal, Computational Modeling of Intracellular Ca²⁺ Signals
740 in Astrocytes. *Encyclopedia of Computational Neuroscience* p. Submitted (2019). Sub-
741 mitted.
- 742 60. M. M. Wu, J. Buchanan, R. M. Luik, R. S. Lewis, Ca²⁺ store depletion causes STIM1 to
743 accumulate in ER regions closely associated with the plasma membrane. *J Cell Biol* **174**,
744 803–813 (2006).

- 745 61. H. Wu, P. Carvalho, G. K. Voeltz, Here, there, and everywhere: The importance of ER
746 membrane contact sites. *Science* **361**, eaan5835 (2018).
- 747 62. C. Escartin, *et al.*, Reactive astrocyte nomenclature, definitions, and future directions. *Nature Neuroscience* pp. 1–14 (2021). Publisher: Nature Publishing Group.
- 749 63. J. R. Jones, L. Kong, M. G. Hanna, B. Hoffman, R. Krencik, R. Bradley, T. Hagemann,
750 J. Choi, M. Doers, M. Dubovis, M. A. Sherafat, A. Bhattacharyya, C. Kendzierski, A. Au-
751 dhya, A. Messing, S.-C. Zhang, Mutations in GFAP Disrupt the Distribution and Function
752 of Organelles in Human Astrocytes. *Cell Reports* **25**, 947–958.e4 (2018).
- 753 64. E. Shigetomi, K. Saito, F. Sano, S. Koizumi, Aberrant Calcium Signals in Reactive As-
754 trocytes: A Key Process in Neurological Disorders. *International Journal of Molecular*
755 *Sciences* **20**, 996 (2019).
- 756 65. T. Manninen, R. Havela, M.-L. Linne, Computational Models for Calcium-Mediated As-
757 trocyte Functions. *Frontiers in Computational Neuroscience* **12** (2018).
- 758 66. A. Denizot, H. Berry, S. Venugopal, Intracellular Calcium Signals in Astrocytes, Computa-
759 tional Modeling of. *Encyclopedia of Computational Neuroscience*, D. Jaeger, R. Jung, eds.
760 (Springer, New York, NY, 2020), pp. 1–12.
- 761 67. K. Breslin, J. J. Wade, K. Wong-Lin, J. Harkin, B. Flanagan, H. V. Zalinge, S. Hall,
762 M. Walker, A. Verkhratsky, L. McDaid, Potassium and sodium microdomains in thin
763 astroglial processes: A computational model study. *PLOS Computational Biology* **14**,
764 e1006151 (2018).
- 765 68. A. Denizot, M. Arizono, V. Nägerl, H. Berry, E. D. Schutter, Astrocyte nanoscale mor-
766 phology controls Ca²⁺ signals at tripartite synapses. *bioRxiv* p. 2021.02.24.432635 (2021).
767 Publisher: Cold Spring Harbor Laboratory Section: New Results.
- 768 69. L. Héja, Z. Szabó, M. Péter, J. Kardos, Spontaneous Ca²⁺ Fluctuations Arise in Thin As-
769 trocytic Processes With Real 3D Geometry. *Frontiers in Cellular Neuroscience* **15** (2021).
770 Publisher: Frontiers.
- 771 70. N. Korogod, C. C. Petersen, G. W. Knott, Ultrastructural analysis of adult mouse neocortex
772 comparing aldehyde perfusion with cryo fixation. *eLife* **4**, e05793 (2015).
- 773 71. M. Arizono, S. Bancelin, P. Bethge, R. Chéreau, A. Idziak, V. V. G. K. Inavalli, T. Pfeif-
774 fer, J. Tønnesen, U. V. Nägerl, Nanoscale imaging of the functional anatomy of the brain.
775 *Neuroforum* (2021). Publisher: De Gruyter Section: Neuroforum.
- 776 72. R. Fernández-Busnadiego, Y. Saheki, P. D. Camilli, Three-dimensional architecture of ex-
777 tended synaptotagmin-mediated endoplasmic reticulum–plasma membrane contact sites.
778 *Proceedings of the National Academy of Sciences* **112**, E2004–E2013 (2015).

- 779 73. T. Cui-Wang, C. Hanus, T. Cui, T. Helton, J. Bourne, D. Watson, K. Harris, M. Ehlers,
780 Local Zones of Endoplasmic Reticulum Complexity Confine Cargo in Neuronal Dendrites.
781 *Cell* **148**, 309–321 (2012).
- 782 74. C. Cali, K. Kare, M. Agus, M. F. V. Castillo, D. Boges, M. Hadwiger, P. Magistretti, A
783 Method for 3D Reconstruction and Virtual Reality Analysis of Glial and Neuronal Cells.
784 *JoVE (Journal of Visualized Experiments)* p. e59444 (2019).
- 785 75. G. W. De Young, J. Keizer, A single-pool inositol 1,4,5-trisphosphate-receptor-based model
786 for agonist-stimulated oscillations in Ca²⁺ concentration. *Proceedings of the National*
787 *Academy of Sciences* **89**, 9895–9899 (1992).
- 788 76. I. Hepburn, W. Chen, S. Wils, E. De Schutter, STEPS: efficient simulation of stochastic
789 reaction–diffusion models in realistic morphologies. *BMC Systems Biology* **6**, 36 (2012).
- 790 77. D. T. Gillespie, Exact stochastic simulation of coupled chemical reactions. *The Journal of*
791 *Physical Chemistry* **81**, 2340–2361 (1977).
- 792 78. Y. Hu, Q. Zhou, X. Gao, A. Jacobson, D. Zorin, D. Panozzo, Tetrahedral meshing in the
793 wild. *ACM Transactions on Graphics* **37**, 60:1–60:14 (2018).
- 794 79. A. Jorstad, B. Nigro, C. Cali, M. Wawrzyniak, P. Fua, G. Knott, NeuroMorph: A Toolset
795 for the Morphometric Analysis and Visualization of 3D Models Derived from Electron
796 Microscopy Image Stacks. *Neuroinformatics* **13**, 83–92 (2015).

797 **Acknowledgements**

798 This work used the computing resources of the Scientific Computing and Data Analysis section
799 from the Okinawa Institute of Science and Technology. We thank Iain Hepburn and Weiliang
800 Chen of the Computational Neuroscience Unit, OIST, Okinawa, Japan for discussion and advice
801 on STEPS software. We thank Pierre Magistretti (KAUST, Thuwal) for the financial support to
802 MFVC and to CC, and Graham Knott for kindly sharing the original EM dataset.

803
804 **Funding:** The work from AD was supported by a JSPS (Japan Society for the Promotion of
805 Science) Standard Postdoctoral Fellowship for Research in Japan (21F21733).

806
807 **Author Contributions** AD, CC and EDS conceived the research, provided resources and su-
808 pervised the work. AD and EDS designed the analysis. MFVC and CC curated the electron
809 microscopy data. PP wrote the Blender code for automatic 3D mesh handling. AD did the com-
810 putational modeling work. AD performed data analysis and visualisation of experimental and
811 computational data. AD wrote the first draft of the manuscript. All authors read and reviewed
812 the manuscript.

813

814 **Competing Interests** The authors declare that they have no competing financial interests.

815

816 **Data and materials availability:** The 3D meshes, geometrical data and code produced in this
817 study will be available online upon paper acceptance.